SÃO PAULO STATE UNIVERSITY
Graduate Program in Mechanical Engineering
Campus Bauru

Wave Propagation in a One-Dimensional Diatomic Periodic Structure with High-Static–Low-Dynamic Stiffness and Prestress Effects

Diego Pereira Vasconcellos

Bauru
2025

Wave Propagation in a One-Dimensional Diatomic Periodic Structure with High-Static–Low-Dynamic Stiffness and Prestress Effects

Diego Pereira Vasconcellos

Thesis presented at São Paulo State University, School of Engineering of Bauru, Postgraduate Program in Mechanical Engineering in the Area of Mechanical Projects, as part of the requirements necessary to obtain the title of Doctor of Mechanical Engineering.

Supervisor: Prof. Dr. Fabricio Cesar Lobato de Almeida

Bauru

2025

Vasconcellos, Diego Pereira.
Wave Propagation in a One-Dimensional Diatomic Periodic Structure with High-Static-Low-Dynamic Stiffness and Prestress Effects / Diego Pereira Vasconcellos. – Bauru, 2025
107 f. : il., tabs.

Tese (Doutorado)–Universidade Estadual Paulista (Unesp), Faculdade de Engenharia, Bauru
Orientador: Fabricio Cesar Lobato de Almeida

1. Bandgap. 2. Dispersion Relation. 3. Geometric Nonlinearity. 4. Mass Ratio. 5. Periodic Structure. 6. Prestress. 7. Wave Propagation. I. Título.

ATA DA DEFESA PÚBLICA DA TESE DE DOUTORADO DE DIEGO PEREIRA VASCONCELLOS, DISCENTE DO PROGRAMA DE PÓS-GRADUAÇÃO EM ENGENHARIA MECÂNICA, DA FACULDADE DE ENGENHARIA - CÂMPUS DE BAURU.

Aos 28 dias do mês de agosto do ano de 2025, às 14h, por meio de Videoconferência, realizou-se a defesa de TESE DE DOUTORADO de DIEGO PEREIRA VASCONCELLOS, intitulada **WAVE PROPAGATION IN A ONE-DIMENSIONAL DIATOMIC PERIODIC STRUCTURE WITH HIGH-STATIC-LOW-DYNAMIC STIFFNESS AND PRESTRESS EFFECTS** . A Comissão Examinadora foi constituída pelos seguintes membros: Prof. Dr. FABRICIO CESAR LOBATO DE ALMEIDA (Orientador(a) - Participação Virtual) do(a) Departamento de Engenharia Mecânica / Faculdade de Engenharia de Bauru - UNESP, Prof. Dr. ADRIANO TODOROVIC FABRO (Participação Virtual) do(a) Departamento de Engenharia Mecânica / Universidade de Brasília - UnB, Prof. Dr. DOUGLAS DOMINGUES BUENO (Participação Virtual) do(a) Departamento de Engenharia Mecânica / Faculdade de Engenharia de Ilha Solteira - UNESP, Prof. Dr. FABIO MAZZARIOL SANTICIOLLI (Participação Virtual) do(a) Sistemas Biomédicos / Fatec Bauru, Prof. Dr. RODRIGO BORGES SANTOS (Participação Virtual) do(a) Engenharia Mecânica / Universidade Federal da Grande Dourados. Após a exposição pelo doutorando e arguição pelos membros da Comissão Examinadora que participaram do ato, de forma presencial e/ou virtual, o discente recebeu o conceito final: APROVADO . Nada mais havendo, foi lavrada a presente ata, que após lida e aprovada, foi assinada pelo(a) Presidente(a) da Comissão Examinadora.

gov.br Documento assinado digitalmente
FABRICIO CESAR LOBATO DE ALMEIDA
Data: 29/09/2025 11:54:23-0300
Verifique em https://validar.iti.gov.br

Prof. Dr. FABRICIO CESAR LOBATO DE ALMEIDA

ACKNOWLEDGEMENTS

This study was funded by the Coordination for the Improvement of Higher Education Personnel (CAPES), process number 88887.487915/2020-00. I also extend my gratitude to the ENVIBRO research group, funded by the São Paulo Research Foundation (FAPESP), for their invaluable support and contributions. I would like do express my heartfelt thanks to the following: UNESP, for providing and enriching environment that fostered my academic growth and development. My supervisors, Professor Marcos Silveira and Fabricio Lobato de Almeida, for their encouragement, dedication, patience, and the knowledge shared throughout the development of this work. I am also grateful to God for the strength and wisdom to complete this stage, to my family, to the NDE research group, and especially to my partner Ana Carolina for all the support and encouragement during this period.

“Educação não transforma o mundo. Educação muda pessoas. Pessoas transformam o mundo.” Paulo Freire

Wave Propagation in a One-Dimensional Diatomic Periodic Structure with High-Static–Low-Dynamic Stiffness and Prestress Effects

Diego Pereira Vasconellos

Abstract - This work investigates wave propagation in a one-dimensional diatomic periodic structure with high static and low dynamic stiffness (HSLDS), subjected to different prestress conditions. Such structures exhibit bandgaps, frequency ranges in which wave propagation is suppressed, which are particularly relevant for vibration attenuation in lightweight systems like aerospace and automotive applications. The aim is to understand how geometric nonlinearity and prestress affect the formation and shifting of bandgaps, as well as low-frequency attenuation, with special emphasis on sensitivity to initial conditions analysed through basin of attraction studies. The methodology combines approaches such as mechanical impedance, dispersion relation, fourth-order Runge-Kutta integration, numerical continuation with MatCont, Poincaré sections, Lyapunov exponents, and basins of attraction. Linear results show that the mass ratio and number of unit cells strongly influence bandgaps, with good agreement between transmissibility and dispersion. In the nonlinear regime, prestress significantly alters the dynamics: under compression, quasi-periodic and chaotic responses prevail, while under tension, periodic responses dominate. The basins of attraction revealed multistability and coexistence of regimes, highlighting their importance in predicting dynamic behavior. It is concluded that prestress is an effective strategy for modifying bandgaps and attenuating low-frequency vibrations, representing a promising passive control technique. Moreover, the basin of attraction analysis stands out as a major contribution of this work, by demonstrating how sensitivity to initial conditions affects the predictability of nonlinear periodic structures.

Keywords: Bandgap, Dispersion Relation, Geometric nonlinearity, Mass ratio, Periodic Structure, Prestress, Wave propagation.

Propagação de Ondas em uma Estrutura Periódica Diatômica Unidimensional com Rigidez Estática Alta e Dinâmica Baixa e Efeitos de Pré-Carga

Diego Pereira Vasconellos

Resumo - Este trabalho investiga a propagação de ondas em uma estrutura periódica unidimensional diatômica com rigidez estática elevada e dinâmica reduzida (HSLDS), submetida a diferentes condições de pré-carga. Essas estruturas apresentam bandgaps, regiões de supressão de ondas relevantes para atenuação de vibrações em sistemas leves, com aplicações aeroespaciais e automotivas. O objetivo é compreender como a não linearidade geométrica e a pré-carga afetam a formação e o deslocamento dos bandgaps, bem como a atenuação em baixas frequências, com atenção especial à sensibilidade às condições iniciais analisada por meio das bacias de atração. A metodologia combina análises como: impedância mecânica, relação de dispersão, Runge-Kutta de quarta ordem, continuação no MatCont, seção de Poincaré, expoente de Lyapunov e bacias de atração. Os resultados lineares mostram que a razão de massa e o número de células unitárias influenciam os bandgaps, com boa concordância entre transmissibilidade e dispersão. No regime não linear, a pré-carga altera a dinâmica: sob compressão, predominam respostas quase-periódicas e caóticas, enquanto sob tração surgem respostas mais periódicas. As bacias de atração revelaram multistabilidade e coexistência de regimes, destacando sua importância para prever o comportamento dinâmico. Conclui-se que a pré-carga é uma estratégia eficaz para modificar bandgaps e atenuar vibrações em baixas frequências, podendo ser utilizada como uma técnica de controle passivo, e que a análise da bacia de atração constitui uma importante contribuição deste trabalho ao evidenciar a influência das condições iniciais na previsibilidade de estruturas periódicas não lineares.

Palavras-chave: Bandgap, Relação de dispersão, Não linearidade geométrica, Razão de massa, Estrutura periódica, Pré carga, Propagação de ondas.

CONTENTS

LIST OF FIGURES

NOMENCLATURE

Designation	Explanation
Latin symbols	
A	Perturbation amplitude in the dispersion relation
a	Angular coefficient of the line
c	Damping coefficient
F_0	Amplitude of the external force
i	Imaginary unit
Im	Imaginary part
k_a	Stiffness coefficient of the transversal spring
K_L	Linear stiffness coefficient
K_{NL}	Nonlinear stiffness coefficient
L	Final length
L_0	Undeformed spring length
L_i	Initial length
m_1, m_2	Mass coefficients
P	Prestress
Re	Real part
T	Transmissibility
u	Auxiliary variable representing $\cos(\omega t)$ in the Hopf normal form
$\dot{u}$	Time derivative of u

$u_{j,1}$, $u_{j,2}$	Displacement of masses m_1 and m_2, respectively
v	Auxiliary variable representing $\sin(\omega t)$ in the Hopf normal form
$\dot{v}$	Time derivative of v
x	Displacement
$\dot{x}$	Velocity
$\ddot{x}$	Acceleration
y	Displacement in state variables
$\dot{y}$	Time derivative of y
$\mathbf{C}$	Damping matrix
$\mathbf{G}(\mathbf{x})$	Vector of nonlinear terms
$\mathbf{K}$	Stiffness matrix
$\mathbf{M}$	Mass matrix
Z	Mechanical impedance
$\ddot{u}_{j,1}, \ddot{u}_{j,2}$	Acceleration of masses m_1 and m_2, respectively
Greek symbols	
ϵ	Dimensionless parameter representing the degree of nonlinearity
η	Amplitude ratio
κ	Wavenumber
λ	Lyapunov exponent
μ	Mass ratio
ω	Excitation frequency
$\bar{\omega}$	Nondimensional frequency
ω_a, ω_b, ω_c	Frequencies where the transmissibility magnitude of the linear cell is equal to 1
ω_1, ω_2, ω_3	Natural frequencies of the linear cell

ω_n	Natural frequency
τ	Nondimensional time
θ	Angle between the initial and final position of m_2
Abbreviations	
cc	Complex Conjugate
HSLDS	High-Static–Low-Dynamic Stiffness

Chapter 1

INTRODUCTION

This chapter outlines the motivation behind this thesis, provides a review of the literature concerning periodic structures and nonlinear behaviour, and presents the problem statement, research objectives, key contributions, and the overall structure of the thesis.

1.1 Motivation

Vibrations are often undesirable in engineering systems, as they can lead to performance degradation, discomfort, structural fatigue, and even failure. In applications such as aerospace, automotive, civil infrastructure, and precision manufacturing, the control and attenuation of vibrations are essential to ensure functionality, safety, and longevity (INMAN; SINGH, 1994; RAO, 2011). The need for effective vibration mitigation becomes even more critical when operating under dynamic loads or in environments where added mass, size, or energy consumption must be minimized. This ongoing challenge has driven the development of advanced strategies for passive, active, and semi-active control techniques.

Among the passive solutions, periodic structures have emerged as a promising approach due to their ability to manipulate wave propagation through the formation of bandgaps—frequency ranges in which wave transmission is inhibited.

Periodic structures have gained significant attention across multiple engineering domains due to their ability to manipulate wave propagation phenomena. Their inherent periodicity gives rise to bandgaps—frequency ranges in which wave transmission is suppressed—making them highly effective for applications in vibration isolation, wave filtering, and energy localization (MEAD, 1996; HUSSEIN; LEAMY; RUZZENE, 2014; SUGINO; RUZZENE; ERTURK, 2018; VASCONCELLOS; SILVEIRA, 2020; VASCONCELLOS *et al.*, 2022). Such structures are employed in aerospace, mechanical, civil, and naval engineering, where vibration control is essential for performance, durability, and safety.

Traditional linear approaches to vibration attenuation often require either added mass, such as dynamic vibration absorbers or tuned mass dampers, or extreme compliance, for instance through very soft suspension systems or flexible supports, to be effective in the low-frequency regime. To overcome this limitation, recent research has focused on the inclusion of nonlinear elements within periodic architectures. These nonlinear mechanisms, particularly of geometric or stiffness-based origin, offer passive tunability of system dynamics, enabling enhanced control over the frequency response and the possibility of broadband or adaptive attenuation (VAKAKIS; KING, 1998; POPA; CUMMER, 2014; MEAUD, 2020).

A notable strategy in this context is the use of high static–low dynamic stiffness (HSLDS) mechanisms, which allow for strong static load-bearing capacity combined with reduced dynamic stiffness. This makes it possible to isolate low-frequency vibrations while maintaining a compact and lightweight design—an essential feature in aerospace and precision systems (CARRELLA; BRENNAN; WATERS, 2007; HAO; CAO, 2015). Furthermore, given the sensitivity of nonlinear systems to initial conditions, it is crucial to investigate their influence. One effective approach is through stability analysis using basins of attraction (SOLIMAN; THOMPSON, 1989; LENCI; REGA; RUZZICONI, 2013; ORLANDO *et al.*, 2019).

Given the increasing demand for adaptive, lightweight, and multifunctional systems,

the study of periodic structures with nonlinear stiffness profiles—especially those exhibiting HSLDS behaviour —represents a promising research direction. The present work focuses on a diatomic, geometrically nonlinear periodic structure, aiming to analyse its transmissibility, dispersion relations, dynamic regimes and stability through basin of attraction analysis. This approach builds upon recent advances in the field and contributes to a deeper understanding of nonlinear wave propagation in engineered materials.

1.2 Literature Review

In this section definitions and different studies of topics related to this thesis are presented, topics such as: periodic structures, analytical methods, numerical analysis and nonlinear terms.

1.2.1 Periodic Structures

According to Mead (1996), a periodic structure fundamentally consists of a number of identical structural components connected side by side to form a larger assembly and can be classified as one-, two-, or three-dimensional (1D, 2D, or 3D). The study of periodic structures, often referred to as metamaterials, began with the work of Veselago (1968), who discovered materials exhibiting negative electric permittivity, magnetic permeability, and refractive index. This concept was later extended to the fields of acoustics and vibration through the use of negative effective mass, typically implemented by adding dynamic vibration absorbers.

Periodic structures can consist of beams, bars, flat plates, or curved shells in various combinations and with different support conditions. Figure 1.1 from Sugino *et al.* (2017) shows some examples of periodic structures, such as a shaft under torsional/longitudinal excitation (a), a bar under transverse excitation (b), and a plate under transverse excitation (c).

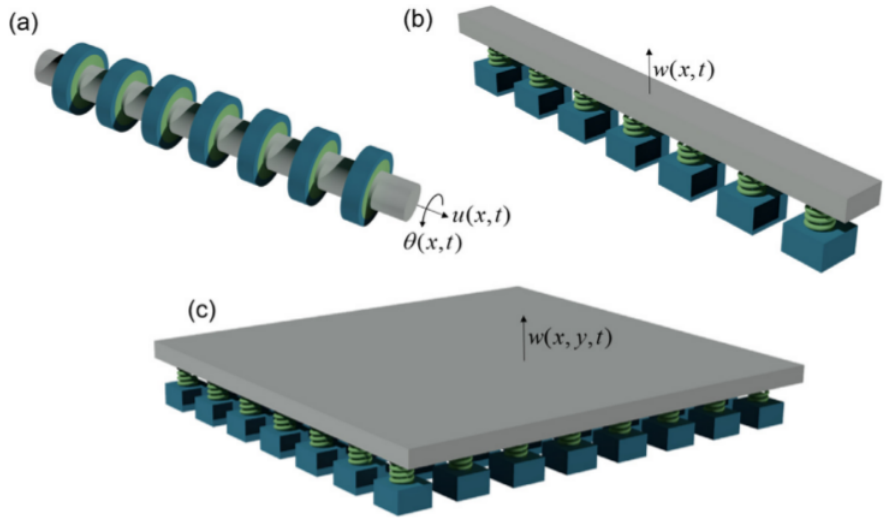

Figure 1.1: Examples of periodic structures, where (a) is a shaft under torsional/longitudinal excitation, (b) is a bar under transverse excitation, and (c) is a plate under transverse excitation. Source: Sugino *et al.* (2017)

Due to the inherent periodicity of these systems, unique dynamic behaviours can emerge, such as the formation of bandgaps. The concept of bandgaps, originally introduced in the context of wave propagation in periodic media, refers to frequency ranges in which wave transmission is inhibited due to destructive interference caused by the medium's periodicity. This phenomenon was rigorously investigated by Brillouin (1946) in the study of electronic wave propagation in crystal lattices and was later extended to elastic and acoustic waves in engineered periodic structures.

In periodic structures, a bandgap is typically defined as a frequency interval in which wave propagation is forbidden due to scattering mechanisms induced by periodicity (OUDICH *et al.*, 2023). Within this framework, the term stopband is also employed to denote frequency ranges where strong attenuation occurs, often associated with Bragg scattering or local resonance effects, which prevent efficient wave transmission (DING; MAGNUSSON, 2007). It should be noted, however, that the terminology is not always used consistently across the literature, as many authors use bandgap and stopband interchangeably when discussing metamaterials and phononic crystals (CROËNNE *et al.*, 2011; IQBAL *et al.*, 2021).

The theoretical foundation for analyzing wave propagation in such systems is grounded in Bloch's theorem, which states that the wave solutions in a periodic medium can be expressed as a plane wave modulated by a periodic function. This formalism, originally formulated in the context of solid-state physics and extensively discussed in Kittel and McEuen (2018), is essential for deriving the dispersion relations and predicting wave behaviour in periodic structures. It allows the dynamic behaviour of complex periodic systems to be reduced to the analysis of a representative unit cell, significantly simplifying the problem. A comprehensive review of the application of Bloch wave analysis in phononic materials and metamaterials is provided by Hussein, Leamy and Ruzzene (2014), who also explore its implications in vibration attenuation and energy localization.

Narisetti, Leamy and Ruzzene (2010) presented a perturbation-based analytical approach to study wave propagation in one-dimensional infinite nonlinear periodic structures. The authors considered both monoatomic and diatomic configurations and derived dispersion relations to predict the formation of bandgaps. In the linear regime, the dispersion relation revealed the classical behaviour of wave propagation and attenuation due to periodicity. For the diatomic case, an additional bandgap appears due to the contrast in mass and stiffness between neighboring units. The methodology provides fundamental insights into how nonlinearity and periodicity interact to influence the dynamic response and frequency band structure of such systems. Figure 1.2 illustrates the monoatomic and diatomic periodic configurations, as well as the dispersion relation corresponding to the diatomic structure, where a bandgap can be observed between frequencies 1 and 1.4, indicating a range with no wave propagation, where A_0 is the amplitude, Γ is nonlinear parameter and μ is wavenumber.

Periodic structures are of significant interest in various engineering disciplines due to their capacity to control the propagation of mechanical, acoustic, and electromagnetic waves. Their applications range from vibration and noise isolation to seismic impact mitigation and industrial process optimisation. The following studies highlight the rel-

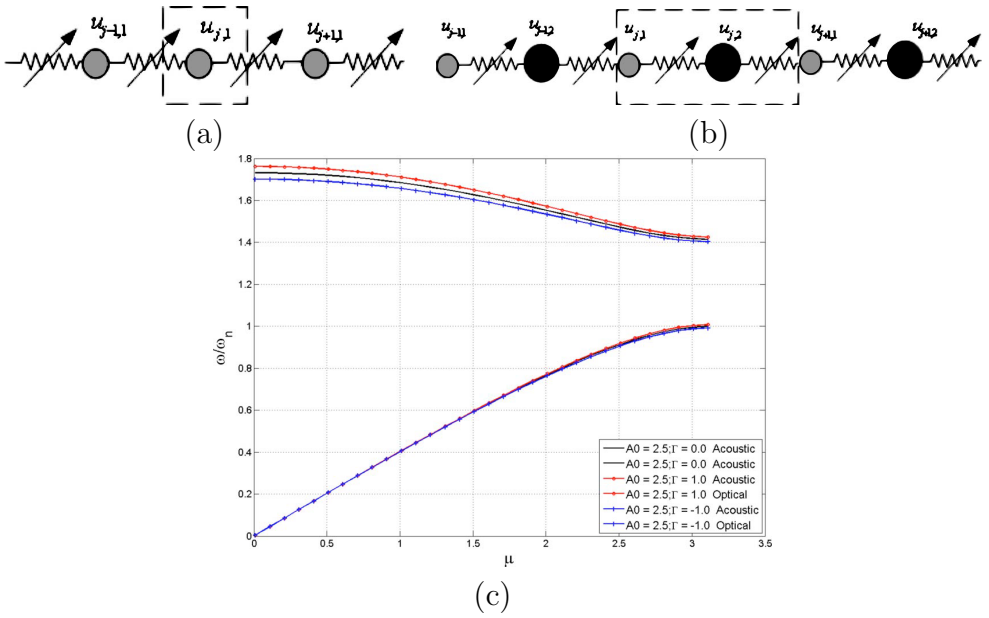

Figure 1.2: Periodic structure: (a) monoatomic configuration; (b) diatomic configuration; (c) dispersion relation corresponding to the diatomic structure, where A_0 is the amplitude, Γ is nonlinear parameter and μ is wavenumber. Source Narisetti, Leamy and Ruzzene (2010)

evance of periodic structures in engineering.

Yao, Zhou and Hu (2008) conducted an experimental study on negative effective mass in a 1D mass-spring system, where they analysed its transmission property at low frequencies and demonstrated the application of this effect. Sugino *et al.* (2017) presented a general theory for estimating bandgaps in locally resonant periodic structures. The authors used a method based on modal analysis to understand the bandgap and demonstrated that periodicity is responsible for the emergence of Bragg bandgaps.

Krödel, Thomé and Daraio (2015) investigated seismic periodic structures designed to create wide bandgaps by leveraging local resonances capable of reflecting acoustic waves with wavelengths much larger than the structure's characteristic size. They proposed a metastructure composed of cylindrical units with suspended resonators, embedded around sensitive buildings, to attenuate seismic waves in the 1–10 Hz range. Complementarily, Gonçalves, Brennan and Cleante (2021) demonstrated that the stopband behaviour of finite mono-coupled periodic structures can be reliably predicted by

analyzing the transmissibility of a single unit cell, providing a valuable tool for the design of compact and efficient metamaterials.

Moreover, Carneiro *et al.* (2021) study the vibration attenuation properties of finite periodic arrays of rods composed of symmetric and asymmetric cells. By analyzing the transmissibility through a single unit cell, they demonstrate that asymmetric configurations outperform symmetric ones in terms of vibration isolation for finite structures. Their results emphasize the importance of cell design in determining the overall attenuation performance of nonlinear periodic systems.

Hobeck, Laurant and Inman (2015) conducted a study on utilizing periodic structures fabricated with 3D printing for vibration attenuation, where the structure is modeled using analytical elements and the Rayleigh quotient is used to estimate the natural frequency of the absorbers. They also employed finite element method software and experimental analysis for validation. They demonstrated the effectiveness of 3D-printed periodic structures for vibration attenuation, even with a simple geometry.

Sugino and Erturk (2018) conducted a study to form multifunctional periodic structures, both to generate low-power electrical energy and to attenuate vibrations. They used an electromechanical metastructure and relied on the Euler-Bernoulli beam theory to model the system. The structure used by them is shown in 1.3.

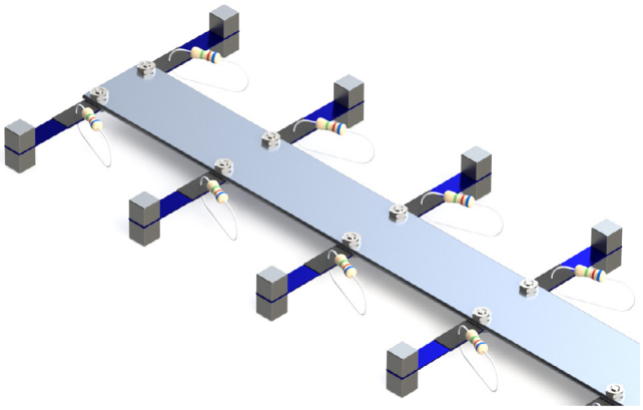

Figure 1.3: Periodic structure used for energy harvesting and vibration attenuation. Source: Sugino and Erturk (2018).

Zhu *et al.* (2014) conducted a study on vibration attenuation within a desired bandgap, employing a matrix of chiral absorbers with a unique design. They used theoretical beam modeling to investigate the bandgap and validated the model through experimental analyses. Hobeck and Inman (2015) introduced the concept of magnetoelastic metastructures for broadband vibration attenuation, which are essentially zigzag-shaped structures. They utilised the Rayleigh-Ritz formulation to model the metastructure and achieved an 84.5% attenuation of the nonlinear periodic structure compared to 41% of the linear one.

There are numerous examples of periodic structures in engineering, such as a building with multiple identical floors, bridges with multiple spans, turbines with multiple blades, aerospace, and naval structures (MEAD, 1996). In the design of these structures, vibration levels must be taken into consideration, both due to the equipment's operation and external forces. These studies demonstrate the versatility of periodic structures and their broad applicability across engineering domains, particularly in vibration attenuation, energy harvesting, and wave manipulation.

1.2.2 Nonlinear Terms

According to Manktelow (2013), the search of a broader range of dynamic responses in periodic structures motivates investigations into the effects of nonlinear behaviour. The incorporation of nonlinear elements within the unit cells offers a passive means of tuning the structural response. Numerous studies explore this theme: Chakraborty and Mallik (2001) analyse the dynamics of a weakly nonlinear periodic chain with both hardening and softening behaviours, employing a perturbation method to investigate wave propagation and attenuation. Similarly, Marathe and Chatterjee (2006) examine wave attenuation in periodic structures incorporating nonlinear damping, using the harmonic balance and multiple scales methods. The structure analysed in their study is shown in figure 1.4, where m denotes the mass, k the stiffness, and ϵ the nonlinear damping

coefficient.

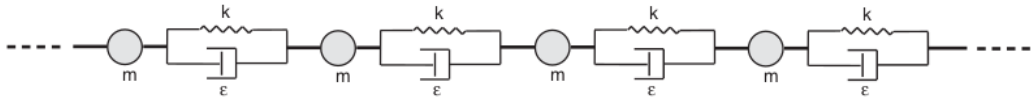

Figure 1.4: Periodic structure with nonlinear damping. Source: Marathe and Chatterjee (2006).

Rothos and Vakakis (2009) investigate strongly nonlinear wave interactions in a linear mass-spring chain, while Boechler *et al.* (2010) develop a novel perturbation approach to predict bandgap location and extent based on both linear and nonlinear system parameters. Yun *et al.* (2005) study the propagation of nonlinear acoustic waves in a one-dimensional periodic medium. In turn, Narisetti, Leamy and Ruzzene (2010) analyse dispersion relations in one- and two-dimensional granular media, revealing frequency bands with wave radiation. These studies highlight the potential of nonlinear periodic structures for designing devices such as acoustic signal processors, filters, diodes, vibration isolators, and energy harvesters.

In the context of acoustic metamaterials, the main objective is to understand and harness the influence of nonlinear behaviour on material behaviour (POPA; CUMMER, 2014). In some instances, nonlinear periodic structures may exhibit chaotic dynamics. For example, Vakakis and King (1998) study standing wave oscillations in an infinite periodic system with cubic nonlinearity, identifying sensitive dependence on initial conditions near the coupling limit—suggesting the emergence of spatial chaos. According to Manktelow (2013), continuous periodic systems are less frequently studied due to the complexities associated with nonlinear partial differential equations and geometrically intricate domains.

Nonlinear behaviour can also arise from specific spring configurations or electromagnetic interactions. For instance, Carrella *et al.* (2009) propose a quasi-zero-stiffness (QZS) isolator composed of a vertical linear spring and two oblique springs, which may

be linear, prestressed, or possess nonlinear softening characteristics. Their results show improved isolation performance when using prestressed springs. The QZS isolator model is shown in Figure 1.5, where I represents linear springs, II linear springs with prestress, and III nonlinear softening springs with prestress. The linear stiffness coefficients are k_1 and k_2, while k_3 corresponds to the nonlinear stiffness. The parameters a and h define the geometry, x the displacement, δ the compression length, and f the applied force.

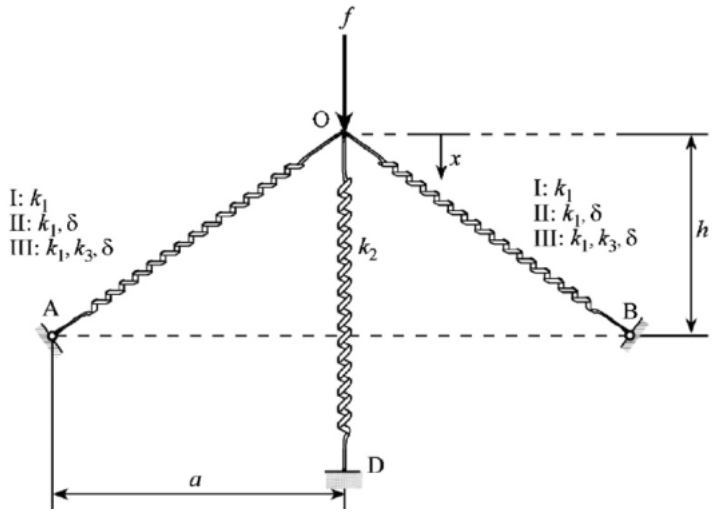

Figure 1.5: Quasi-zero-stiffness (QZS) isolator: I – linear springs, II – linear springs with prestress, III – nonlinear softening springs with prestress. The vertical spring is linear. Source: Carrella *et al.* (2009).

Periodic structures designed with high static–low dynamic stiffness (HSLDS) have gained attention for their ability to combine strong static load-bearing capacity with low dynamic stiffness, making them particularly effective for passive vibration isolation in the low-frequency regime. This configuration allows for the suppression of vibrations near zero frequency without requiring large masses or high structural compliance, which is particularly advantageous for lightweight systems such as aerospace and precision equipment (CARRELLA; BRENNAN; WATERS, 2007; XU *et al.*, 2013; NIU *et al.*, 2014; CHENG *et al.*, 2017; MA; ZHOU; YANG, 2022). Additionally, HSLDS-based structures can be tailored to exhibit broadband attenuation and tunable band gaps through geometric or material nonlinearity (YOUNESIAN; SADRI; ESMAILZADEH,

2014; TANG; BRENNAN, 2014; BAE; OH, 2022).

According to Hao and Cao (2015), a single-degree-of-freedom (SDOF) geometrically nonlinear oscillator with HSLDS characteristics is capable of supporting high static loads while providing dynamic isolation. The authors use an extended averaging method to optimize parameters for maximum isolation bandwidth, and demonstrate through simulations the presence of rich nonlinear behaviour, including periodic and chaotic responses and the coexistence of multiple solutions.

Tang and Brennan (2014) analyse a vibration isolator with high static-low dynamic stiffness (HSLDS) characteristics under shock excitation and demonstrate that nonlinearity enhances shock attenuation, particularly for low input amplitudes. In a related study, Ledezma-Ramirez *et al.* (2015) conduct experiments using electromagnetic and permanent magnets to induce nonlinear stiffness, confirming that such nonlinear behaviour outperform linear elastic elements in shock isolation.

Further exploring this field, Lamarque, Savadkoohi and Charlemagne (2018) present an experimental study involving a 3D-printed periodic structure with HSLDS-type springs, targeting passive vibration control. Their structure is depicted in figure 1.6.

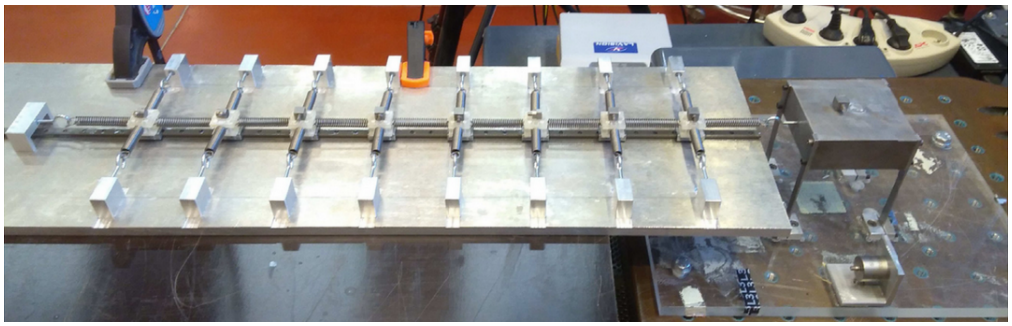

Figure 1.6: 3D-printed periodic structure with HSLDS (high static–low dynamic stiffness) springs. Source: Lamarque, Savadkoohi and Charlemagne (2018).

Further exploring the application of HSLDS to wave control, Wang *et al.* (2019) investigate a locally resonant rod equipped with an HSLDS resonator to generate low-frequency band gaps for longitudinal wave propagation. Their results show that while damping influences the depth and width of the band gap, the nonlinearity of the system

affects its central frequency and bandwidth, enabling effective control of vibrational energy even at very low frequencies. Figure 1.7 show the diagram used, where (a) is the rest configuration, (b) deformed configuration and (c) free-body diagram.

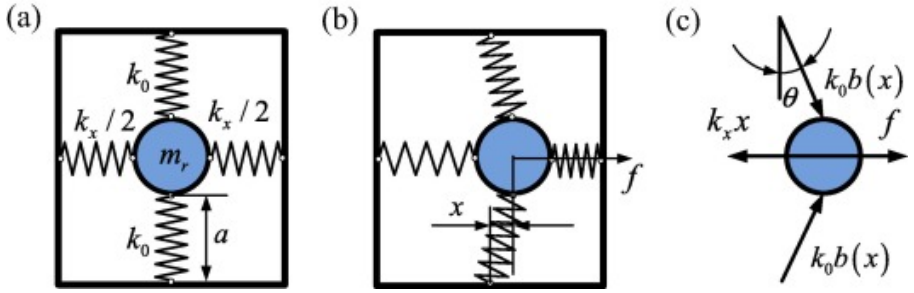

Figure 1.7: Schematic diagram of static analysis of the HSLDS resonator. Source: Wang *et al.* (2019).

The study by Hao, Cao and Wiercigroch (2017) examines the nonlinear dynamics of a harmonically excited QZS-SD (Smooth and Discontinuous) oscillator composed of a lumped mass connected to a vertical spring with positive stiffness and a pair of horizontally compressed springs with negative stiffness. The authors conduct detailed bifurcation analyses and numerical simulations to reveal both local and global dynamic behaviour, highlighting the complex response scenarios induced by the geometric nonlinearity.

Geometric nonlinearity is also exploited in elastic metamaterials to enable tunable wave control. Bae and Oh (2022) propose a periodic structure with nonlinear springs, aiming to create a quasi-static, frequency-adjustable band gap starting from zero frequency. By manipulating the amplitude of excitation and the spring lengths, they achieve control over a negative effective mass region, which precisely coincides with the range where the band gap is formed. This finding emphasizes the role of geometric nonlinearity in enabling adaptive or reconfigurable metamaterials.

To explore isolation techniques at quasi-static frequencies, an approach employing isolators with high static stiffness and low dynamic stiffness (HSLDS) characteristics was adopted. Recent studies have shown that Quasi-Zero Stiffness (QZS) isolators are effective in this context. For example, Sui *et al.* (2023) proposed a QZS isolator based

on an inclined trapezoidal beam, achieving an initial natural frequency of 2.91 Hz. Additionally, Xiao *et al.* (2024) developed a 3D-printed QZS isolator, highlighting its effectiveness in low-frequency vibration environments. These studies indicate that, by properly adjusting structural parameters, very low natural frequencies can be achieved, suitable for sub-Hertz isolation.

Building on these concepts, in this thesis geometric nonlinearity is introduced through the addition of transverse springs to the periodic structure. By applying different pre-stress conditions to these springs, the objective is to effectively attenuate distinct frequency bands, including the quasi-static region, as highlighted in the literature. Consequently, the parameters used throughout this thesis are chosen to target low-frequency regimes, consistent with the strategies demonstrated in QZS and HSLDS designs.

.

1.3 Problem Statement

Based on the literature review presented, it is evident that periodic structures can be effectively used to attenuate vibrations, and that nonlinear effects — particularly geometric — can enhance attenuation regions and influence the quasi-static behaviour of such systems. This work aims to explore the application of nonlinear periodic structures under axial harmonic excitation, with a focus on analysing displacement transmissibility and dispersion relations. Additionally, the nonlinear behaviour of the periodic structure is investigated through phase planes, Poincaré sections, Lyapunov exponents, and basin of attraction maps.

Figure 1.8 shows the periodic structure analysed in this thesis. In Figure 1.8(a), the dashed line outlines a unit cell with three degrees of freedom, which, when connected to adjacent cells, forms the full periodic structure. Figure 1.8(b) presents a diatomic cell used in the analysis of the infinite periodic structure. The potential and implications of using a diatomic representation are further explored in Chapter 4. The transverse

spring, characterized by the stiffness coefficient k_a, is responsible for introducing the geometric nonlinearity that will be explored in this thesis and serves as the element through which different prestress conditions are applied.

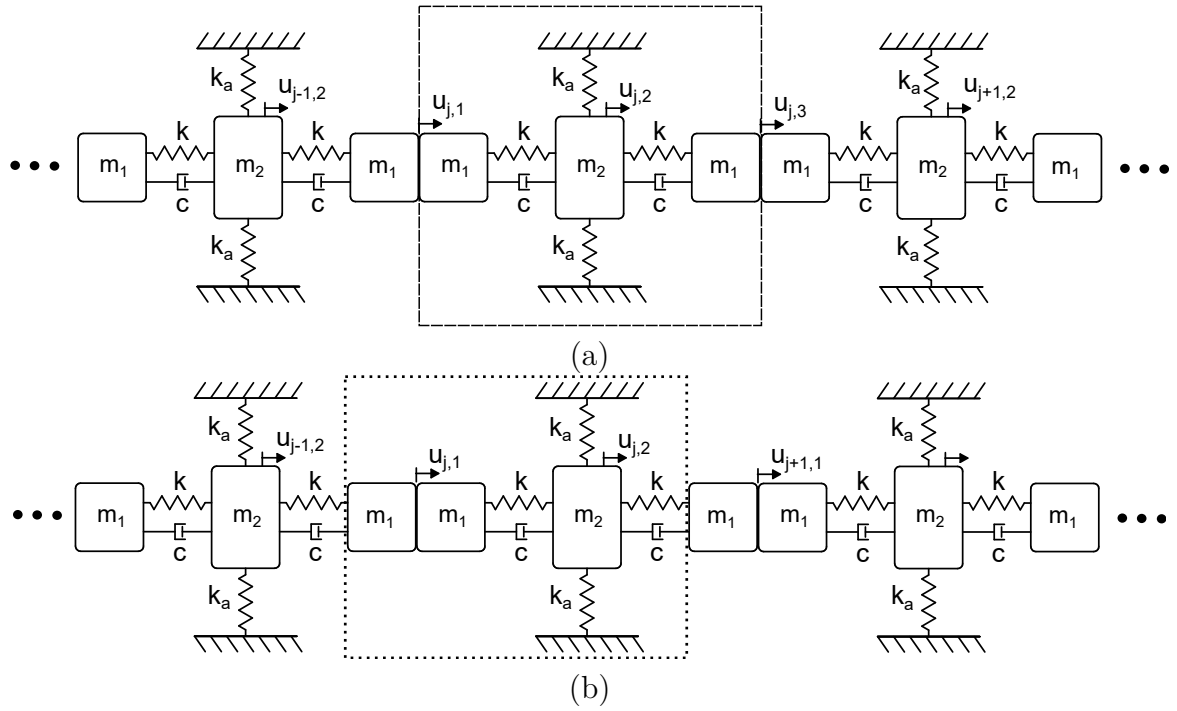

Figure 1.8: A model representing infinite periodic structure with (a) dashed line indicating a cell with three degrees of freedom and (b) dotted line indicating a periodicity of two degree of freedom.

To apply the proposed methodology, we first develop a mathematical model of the system. The dynamical equations are derived based on Newton's second law. We adopt different solution strategies depending on the linearity of the system, and compare the results from both approaches for validation. For the linear case, we use the mechanical impedance method. For the nonlinear case, we perform time-domain integration using the fourth-order Runge-Kutta method and apply continuation techniques implemented in MatCont (DHOOGE *et al.*, 2008). MatCont is a well-established software for bifurcation analysis of nonlinear dynamical systems, enabling the numerical tracking of equilibrium solutions and periodic orbits as system parameters vary. According to Dhooge *et al.* (2008), its implementation combines numerical continuation methods with bifurcation detection algorithms, thus allowing a systematic exploration of stability and

transitions between different dynamical regimes. The numerical continuation technique, which is central to MatCont, consists in following the evolution of solutions as a parameter changes, making it possible to identify critical points such as Hopf bifurcations, period-doubling, or local instabilities. This approach is described by Nayfeh and Balachandran (2008), who presents continuation as a predictor–corrector process in which, starting from a known solution, the solution path is gradually extended, ensuring the construction of complete response branches. Hence, MatCont integrates the theoretical foundation of continuation with its computational implementation, providing a robust platform for the detailed analysis of complex nonlinear systems.

The dispersion relation is obtained following the approach presented in Narisetti, Leamy and Ruzzene (2010). Finally, we construct and analyse the basins of attraction using classification techniques based on FFT, spectral entropy Inouye *et al.* (1991), and effective bandwidth Huang *et al.* (1998). By analysing the basins of attraction in nonlinear periodic structures, we gain deeper insights into multistability and sensitivity to initial conditions in such systems. Studies such as those by Narisetti, Leamy and Ruzzene (2010) and Romeo and Rega (2015) illustrate the complex dynamics that emerge from nonlinear behaviour in periodic structures. We also draw on tools like basin entropy, introduced by Daza, Wagemakers and Sanjuán (2022), and automated methods for estimating basins of attraction, as proposed by Datseris and Wagemakers (2022), which offer effective ways to map and quantify these regions in phase space.

1.4 Objectives

The main objective of this thesis is to analyse the dynamic behaviour of periodic structures with HSLDS-type stiffness under axial excitation, with a focus on enhancing wave attenuation in the bandgap and quasi-static region. The specific objectives are:

1. To develop an analytical model of the periodic structure to characterize and adjust its wave attenuation regions;

2. To analyse the influence of varying mass ratios on the dynamic responses of the periodic structure;

3. To evaluate the impact of different prestress conditions on the formation and shifting of bandgaps and quasi-static regions;

4. To examine the system's sensitivity to initial conditions, with particular attention to the emergence of chaotic and quasi-periodic behaviours;

5. To conduct a basin of attraction analysis to map the dependence of asymptotic system responses on initial conditions, enabling the classification of dynamic regimes and the identification of multistability phenomena.

1.5 Contributions to Knowledge

1. Comprehensive Characterization of Nonlinear Dynamic Behaviour in Periodic Structures:

   This thesis provides a detailed analysis of nonlinear responses in finite periodic structures under varying prestress conditions and mass ratios. By employing time-domain simulations, Poincaré sections, Lyapunov exponents, and spectral analysis, the study classifies dynamic regimes (periodic, quasi-periodic, and chaotic) and highlights the sensitivity of the system to initial conditions.

2. Integration of Dispersion Relation and Transmissibility for Nonlinear Systems:

   A novel comparison between nonlinear dispersion relations (infinite structures) and transmissibility curves (finite structures) is developed, revealing how nonlinear effects — particularly prestress — alter wave propagation, bandgap position, and stability. This dual approach bridges the gap between local unit-cell analysis and global system response.

3. Influence of Prestress and Mass Ratio on Wave Attenuation and Stability:

The research demonstrates how compression and tension prestress affect effective stiffness, equilibrium position, and the resulting vibration attenuation behaviour. The mass ratio is shown to modulate both the emergence of bandgaps and the likelihood of unstable or chaotic responses, enriching the understanding of design parameters in metamaterials.

1.6 Thesis Structure

This thesis is structured as follows: In Chapter 1, a literature review is presented, providing the contextualization of the thesis, where studies and definitions on periodic structures and nonlinearity in periodic structures are discussed. Chapter 2 presents the system modeling to demonstrate how the dynamic equations and system parameters were obtained. Chapter 3 illustrates the analysis of the finite periodic structure, focusing on natural frequencies, vibration modes, and displacement transmissibilities to evaluate the bandgaps, as well as a dynamic analysis through basins of attraction, Poincaré sections, and Lyapunov exponents. Chapter 4 shows the analysis of the infinite periodic structure, examining dispersion relations compared to transmissibilities. Conclusions are presented in Chapter 5.

Chapter 2

MATHEMATICAL MODEL

This chapter introduces the mathematical model of the periodic structure analysed in this thesis, along with some system parameters. The model is developed as follows: first, the equation for the nonlinear term (resulting from the transversal spring) is presented; next, the dependence between terms from the transversal spring is shown, and finally, the dynamical equation is presented in matrix form.

2.1 Periodic Structure Model

Figure 2.1 (a) shows the discrete model of a single cell used to form a periodic structure and figure 2.1 (b) shows a finite periodic structure with two cells, where one cell is coupled next to the other. To finite periodic structure, a harmonic force is applied to the rightmost block, in the form: $F(t) = F_0 \cos(\omega t)$, where F_0 is the force amplitude, ω is the excitation frequency and t is the time. The cell is composed of mass, damping, and stiffness coefficients named m_1, m_2, c, k, and k_a, respectively.

The mass ratio μ is defined as the ratio between m_2 and $2m_1$, according to equation 2.1. In this work, m_1 is fixed at 1, and different values of m_2 are determined by prescribing $\mu = 0.5$, 1, and 2.

$$\mu = \frac{m_2}{2m_1} \tag{2.1}$$

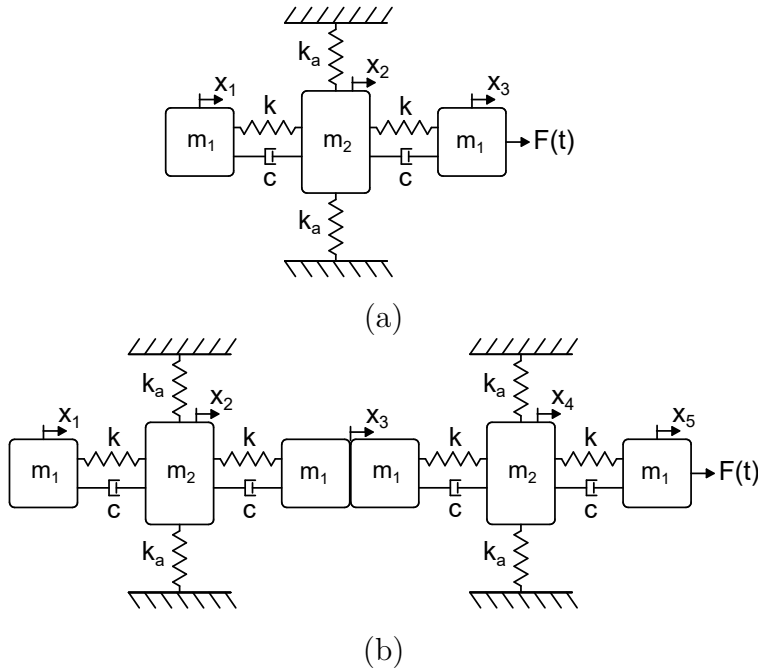

Figure 2.1: A model representing (a) a single cell and (b) a finite periodic structure consisting of two cells.

Figure 2.2 shows the representation of an infinite periodic structure, where a unit cell, illustrated in figure 2.1(a), is infinitely repeated without any external excitation. In figure 2.2(a), a unit cell consisting of three degrees of freedom is outlined with a dashed line. However, due to the inherent periodicity of the structure, an alternative definition of the unit cell is also possible, as indicated by the dotted line in figure 2.2(b), where the cell consists of two degrees of freedom. These two representations are distinct but mathematically equivalent ways of defining the periodic unit cell of the same infinite periodic structure. In Section 4.1, both configurations are considered in the derivation of the dispersion relations, and it is shown that they lead to identical results in the linear case, validating their equivalence. This observation justifies the choice of the two-degree-of-freedom cell for the nonlinear dispersion analysis presented in Section 4.3, as

it allows for a more compact and tractable formulation.

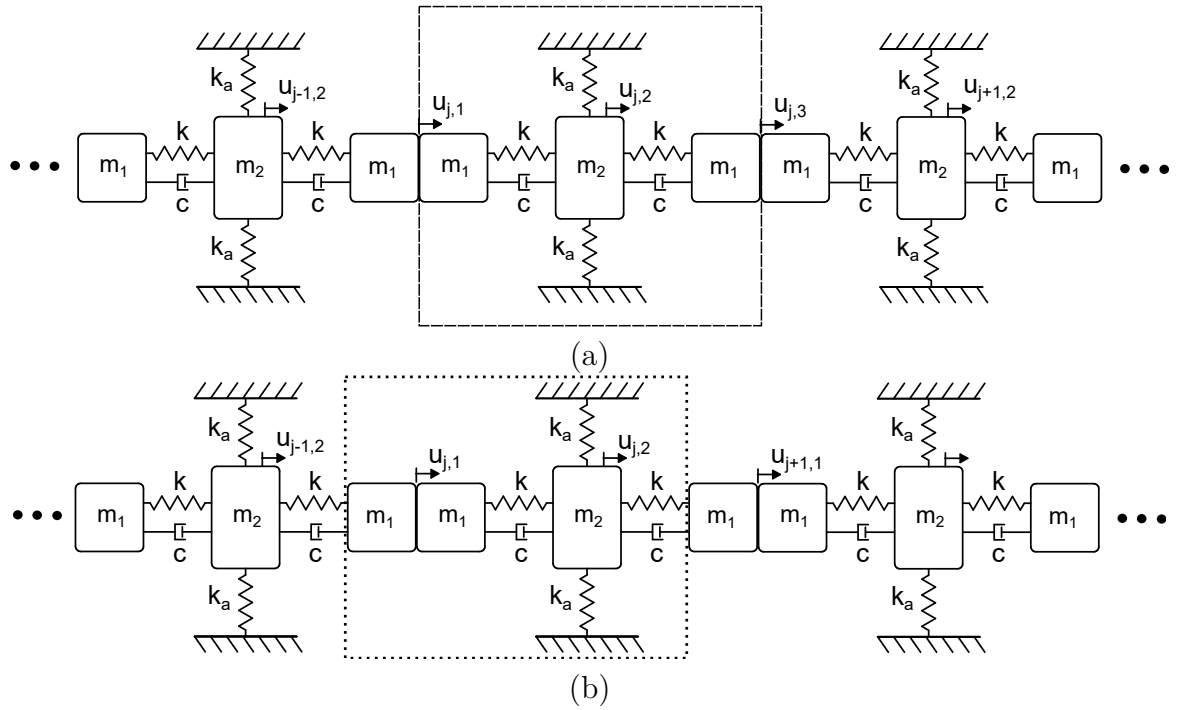

Figure 2.2: Representation of an infinite periodic structure with: (a) unit cell comprising three degrees of freedom (dashed line), and (b) unit cell with two degrees of freedom (dotted line), illustrating two equivalent definitions of periodicity.

Table 2.1 shows the values of mass (m_1), damping (c), and stiffness (k) coefficients utilised in this thesis. In addition to these three parameters, we also have the mass ratio (μ) with three values: 0.5, 1, and 2. These values are chosen to analyse dynamics considering $\mu < 1$, $\mu = 1$, and $\mu > 1$. The force amplitude F_0 is typically set to 1, but in some analyses of the nonlinear system, this amplitude is varied to examine its influence on the system. Parameters related to the transversal spring are detailed in Section 2.3.

Table 2.1: System parameters

m_1 [kg]	c [Ns/m]	k [N/m]
1	0.01	1

2.2 Dynamical Equation of Finite Periodic Structure

Dynamical equations for finite periodic structure shown in figure 2.1(b) are obtained using Newton's second law and can be expressed in general form, with an external harmonic force, as follows:

$$\mathbf{M}\ddot{\mathbf{x}} + \mathbf{C}\dot{\mathbf{x}} + \mathbf{K}\mathbf{x} + \mathbf{G}(\mathbf{x}) = \mathbf{F} \tag{2.2}$$

in which, $\mathbf{M}$ represents the mass matrix, $\ddot{x}$ the acceleration vector, $\mathbf{C}$ the damping matrix, $\dot{x}$ the velocity vector, $\mathbf{K}$ the stiffness matrix, x the displacement vector, $\mathbf{G}(x)$ the vector with nonlinear terms and $\mathbf{F}(t)$ the external force vector.

The displacement vector and the matrices defining equation 2.2 of the periodic structure are given by:

$$\mathbf{M} = \begin{bmatrix} m_1 & 0 & 0 & 0 & 0 & \dots & 0 & 0 \\ 0 & 2\mu m_1 & 0 & 0 & 0 & \dots & 0 & 0 \\ 0 & 0 & m_1 + m_1 & 0 & 0 & \dots & 0 & 0 \\ 0 & 0 & 0 & 2\mu m_1 & 0 & \dots & 0 & 0 \\ 0 & 0 & 0 & 0 & m_1 + m_1 & \dots & 0 & 0 \\ \vdots & \vdots & \vdots & \vdots & \vdots & \ddots & \vdots & \vdots \\ 0 & 0 & 0 & 0 & 0 & \dots & 2\mu m_1 & 0 \\ 0 & 0 & 0 & 0 & 0 & \dots & 0 & m_1 \end{bmatrix}_{(2n+1 \times 2n+1)}$$

$$\mathbf{C} = \begin{bmatrix} c & -c & 0 & 0 & 0 & \dots & 0 & 0 \\ -c & c & -c & 0 & 0 & \dots & 0 & 0 \\ 0 & -c & c + c & -c & 0 & \dots & 0 & 0 \\ 0 & 0 & -c & c & -c & \dots & 0 & 0 \\ 0 & 0 & 0 & -c & c + c & \dots & 0 & 0 \\ \vdots & \vdots & \vdots & \vdots & \vdots & \ddots & \vdots & \vdots \\ 0 & 0 & 0 & 0 & 0 & \dots & c & -c \\ 0 & 0 & 0 & 0 & 0 & \dots & -c & c \end{bmatrix}_{(2n+1 \times 2n+1)} \tag{2.3}$$

$$\mathbf{K} = \begin{bmatrix} k & -k & 0 & 0 & 0 & \dots & 0 & 0 \\ -k & k+K_L & -k & 0 & 0 & \dots & 0 & 0 \\ 0 & -k & k+k & -k & 0 & \dots & 0 & 0 \\ 0 & 0 & -k & k+K_L & -k & \dots & 0 & 0 \\ 0 & 0 & 0 & -k & k+k & \dots & 0 & 0 \\ \vdots & \vdots & \vdots & \vdots & \vdots & \ddots & \vdots & \vdots \\ 0 & 0 & 0 & 0 & 0 & \dots & k+K_L & -k \\ 0 & 0 & 0 & 0 & 0 & \dots & -k & k \end{bmatrix}_{(2n+1\times 2n+1)}$$

$$\mathbf{G} = \begin{bmatrix} 0 & \frac{k_a L_0 x_2^3}{L_i^3} & 0 & \frac{k_a L_0 x_4^3}{L_i^3} & 0 & \dots \frac{k_a L_0 x_{2n}^3}{L_i^3} & 0 \end{bmatrix}^T_{(1\times 2n+1)}$$

$$\mathbf{F} = [0 \;\; 0 \;\; 0 \;\; 0 \;\; 0 \;\; \dots \;\; 0 \;\; F_0 \cos(\omega t)]^T_{(1\times 2n+1)}$$

$$x = [x_1 \;\; x_2 \;\; x_3 \;\; \dots \;\; x_{2n-2} \;\; x_{2n-1} \;\; x_{2n} \;\; x_{2n+1}]^T_{(1\times 2n+1)} \tag{2.4}$$

The following sections explore in greater depth the role of the transverse spring within the proposed framework. Section 2.3 introduces the derivation of its governing equation, providing the basis for the subsequent analysis. Then, in section 2.4, a single-degree-of-freedom system with a transverse spring is investigated as a first step toward understanding its influence under different prestress conditions. This preliminary study also defines the stiffness coefficient k_a and the reference lengths L_i and L_0, which will serve as fundamental parameters throughout the remainder of the thesis.

2.3 Transversal Spring

The spring utilised in the transverse position to the movement is characterized by a stiffness coefficient k_a and a length L_0 when it is disconnected from the system. Figure 2.3(a) shows the spring in its disconnected state from the system. Figures 2.3(b), (c), and (d) shows the spring in scenarios where it is connected to the system, with the spring length denoted as L_i. This spring undergoes three prestresses conditions during the analyses: the condition with no prestress where $L_i = L_0$ (Figure 2.3(b)), compression prestress condition where $L_i < L_0$ (Figure 2.3(c)), and tension prestress condition where $L_i > L_0$ (Figure 2.3(d)).

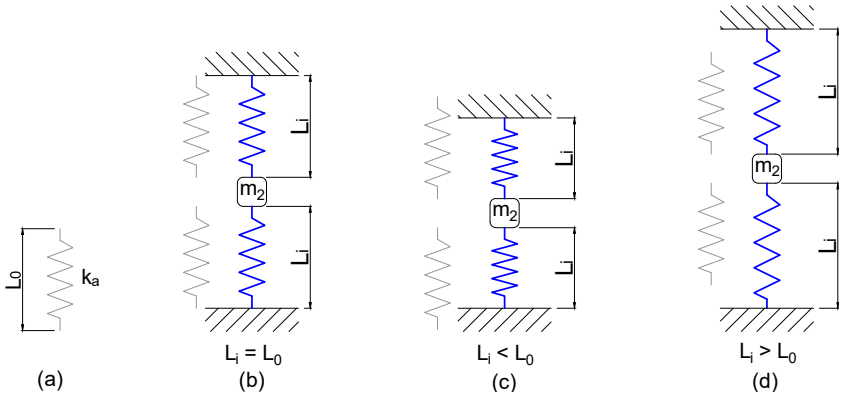

Figure 2.3: Transverse spring (a) disconnected from the system with length L_0 and connected to the system with length L_i: (b) without prestress, (c) compression prestress and (d) tension prestress.

For small displacements of the m_2 mass in the x direction, there is no influence of the transversal spring. For large displacements, a nonlinear restoring force is present due to geometric arrangement. Figure 2.4 shows the geometric effect in the transversal spring with stiffness coefficient k_a under large displacements. In this depiction, figure 2.4 (a) shows the system with tension prestress, while figure 2.4 (b) shows the system with an x displacement, wherein the spring has a length of L. Furthermore, figure 2.4 (c) provides a representation of the free-body diagram for the mass m_2, wherein the red term represents the restoring force in x direction due to the stiffness k_a and the blue represents the restoring force attributed to the prestress.

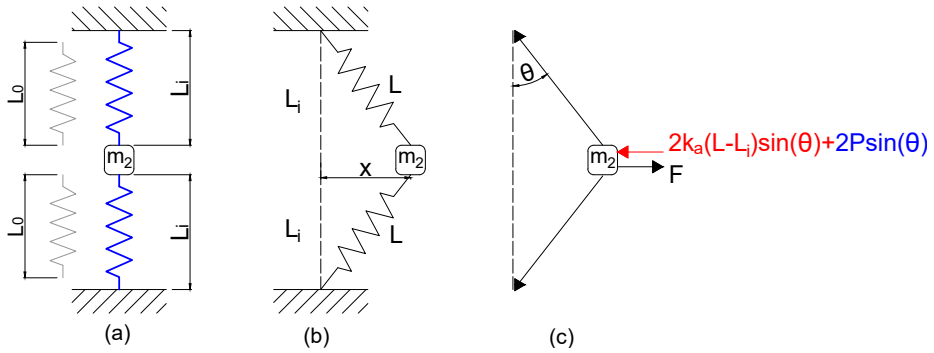

Figure 2.4: Geometric change effect in the transversal spring with stiffness coefficient k_a under large displacements.

The transversal spring is analysed based on its length, and for this purpose, the following nomenclatures are defined: L_0 (undeformed spring length), L_i (initial length), and L (final length). To find the force equation for spring k_a, we consider a tension prestress P, as shown in figure 2.4. By examining the free-body diagram presented, and since the periodic structure's motion is confined to the x direction, the equation for the force F can be expressed as follows:

$$F = 2k_a(L - L_i)\sin(\theta) + 2P\sin(\theta), \tag{2.5}$$

where θ represents the angle between the deformed spring and the horizontal axis. The current length L of the spring, as a function of the horizontal displacement x, is given by:

$$L = \sqrt{L_i^2 + x^2}. \tag{2.6}$$

From this geometric relationship, the sine of the angle θ can be expressed as:

$$\sin(\theta) = \frac{x}{\sqrt{L_i^2 + x^2}}. \tag{2.7}$$

The prestress P, introduced by the elongation of the spring from its natural length L_0 to the initial length L_i, is modeled as:

$$P = 2k_a(L_i - L_0). \tag{2.8}$$

By substituting equations 2.6, 2.7 and 2.8 into equation 2.5, the restoring force can be rewritten in the following closed-form expression:

$$F = \frac{2k_a x}{\sqrt{L_i^2 + x^2}} \left(\sqrt{L_i^2 + x^2} - L_0 \right) \tag{2.9}$$

To facilitate analytical treatment and to capture the system's nonlinear characteristics, the force expression in equation 2.9 is expanded using a Taylor series around $x = 0$, up to the ninth-order term ($\tau = 9$):

$$F = \frac{2k_a(L_i - L_0)x}{L_i} + \frac{L_0 k_a x^3}{L_i^3} - \frac{3L_0 k_a x^5}{4L_i^5} + \frac{5L_0 k_a x^7}{8L_i^7} - \frac{35L_0 k_a x^9}{64L_i^9} \tag{2.10}$$

It is important to note that, in the absence of prestress ($L_i = L_0$), the linear term in the expansion vanishes. Consequently, the force-displacement relationship becomes intrinsically nonlinear, highlighting the role of prestress in tuning the linear stiffness of the system.

Figure 2.5 shows the force-displacement curve and the error compared to the exact equation for displacement. Black curve corresponds to the use of the exact equation

(equation 2.9), while the other curves represent the Taylor series expansion (equation 2.10) up to a certain term: green $\tau = 1$, red $\tau = 3$, magenta $\tau = 5$, blue $\tau = 7$, and olive $\tau = 9$. Dashed lines indicate the point where there is a 0.5% error between the exact curve and each expansion.

Figures 2.5 (a) and (b) show the results for $L_i < L_0$, where a quasi-zero stiffness behaviour can be observed, (c) and (d) consider $L_i = L_0$, and (e) and (f) $L_i > L_0$. In these last two cases, a hardening behaviour can be noticed. Therefore, it can be concluded that the transverse spring exhibits a quasi-zero stiffness behaviour for $L_i < L_0$ and a hardening behaviour for $L_i \geq L_0$.

Given that the expansion up to three terms yields an error of approximately 0.5% up to a displacement of 0.5, it is possible to use this equation to accurately represent the nonlinear term.

2.4 Analysis of Prestress Effects in a Single DOF System with Transversal Spring

To better understand the interplay between the system's components, a single-degree-of-freedom model is first analysed. This simplified system allows for a clearer investigation of the restoring force and dynamics, serving as a foundation for the later analysis of the periodic structure, which constitutes the main focus of this thesis. Figure 2.6 presents the single-degree-of-freedom configuration used to examine how different levels of pre-stress affect the behaviour of the transversal spring.

The equation for the system's restoring force is shown bellow, where, unlike what is commonly seen in a Duffing system, the linear and nonlinear terms are dependents:

$$F = kx + \frac{2k_a(L_i - L_0)}{L_i}x + \frac{k_a L_0}{L_i^3}x^3 \tag{2.11}$$

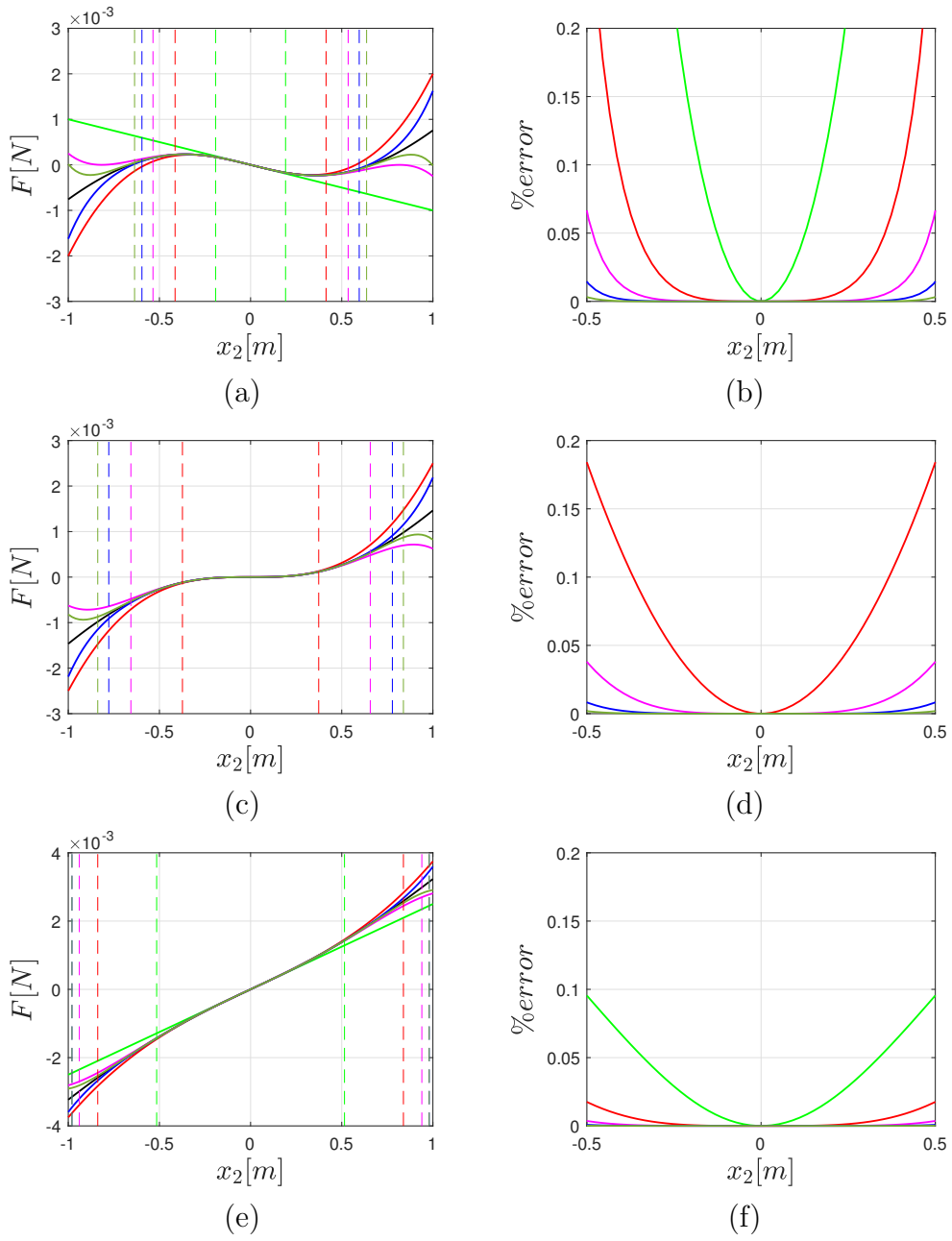

Figure 2.5: Force as function of displacement and error relative to the exact equation by displacement. Figures (a) and (b) show the results for $L_i < L_0$, (c) and (d) with $L_i = L_0$, and (e) and (f) with $L_i > L_0$. The curve represented by — corresponds to the utilization of the exact equation (eq. 2.9), while the other curves represent the utilization of the Taylor series expansion (eq. 2.10) up to a certain term: — $\tau = 1$, — $\tau = 3$, — $\tau = 5$, — $\tau = 7$, and — $\tau = 9$. Dashed lines indicate the point where there is a 0.5% error between the exact curve and each expansion.

To facilitate comparison with the Duffing equation, the linear and nonlinear coefficients are grouped as K_L and K_{NL}, respectively:

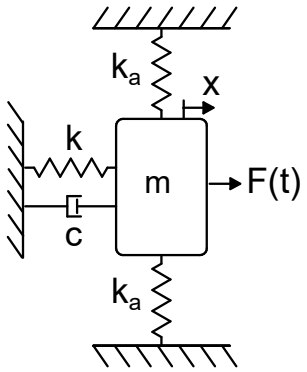

Figure 2.6: Single-degree-of-freedom system used for preliminary analysis of different prestress conditions

$$\begin{aligned} F &= kx + K_L x + K_{NL} x^3 \\ K_L &= \frac{2k_a(L_i - L_0)}{L_i} \\ K_{NL} &= \frac{k_a L_0}{L_i^3} \end{aligned} \tag{2.12}$$

The corresponding dynamical equation becomes:

$$\ddot{x} = (-kx - \frac{2k_a(L_i - L_0)}{L_i}x - \frac{k_a L_0}{L_i^3}x^3 - c\dot{x} + F_0\cos(\omega t))\frac{1}{m} \tag{2.13}$$

To evaluate the dependence between terms K_L and K_{NL}, the stiffness k_a of the transverse spring is rewritten as a function of K_{NL}, L_i and L_0:

$$k_a = \frac{L_i^3}{L_0} K_{NL} \tag{2.14}$$

In addition to rewriting k_a, a function for K_L is also written substituting equation 2.14 into K_L equation 2.12, as follows:

$$K_L = \frac{2L_i^2(L_i - L_0)}{L_0} K_{NL} \tag{2.15}$$

Initially, in order to analyse the transversal spring with a compression prestress, the angular coefficient is evaluated to determine its minimum value while varying L_i and L_0. The angular coefficient is shown below:

$$a = \frac{2L_i^2(L_i - L_0)}{L_0} \tag{2.16}$$

By varying L_i and L_0, the influence of prestress on the linear-nonlinear stiffness relationship can be systematically explored. Figure 2.7(a) illustrates the behaviour of the angular coefficient as a function of the transverse spring length, while figure 2.7(b) shows the variation of K_L as a function of K_{NL}, using the minimum value of the angular coefficient. The highlighted value is selected to assess the influence of prestress on the system's frequency responses. This values is chosen because $|K_L|$ is smaller than k in compression, and since $k = 1$, the chosen values are $K_L = -0.4$, $L_i = 6.667$ and $L_0 = 10$.

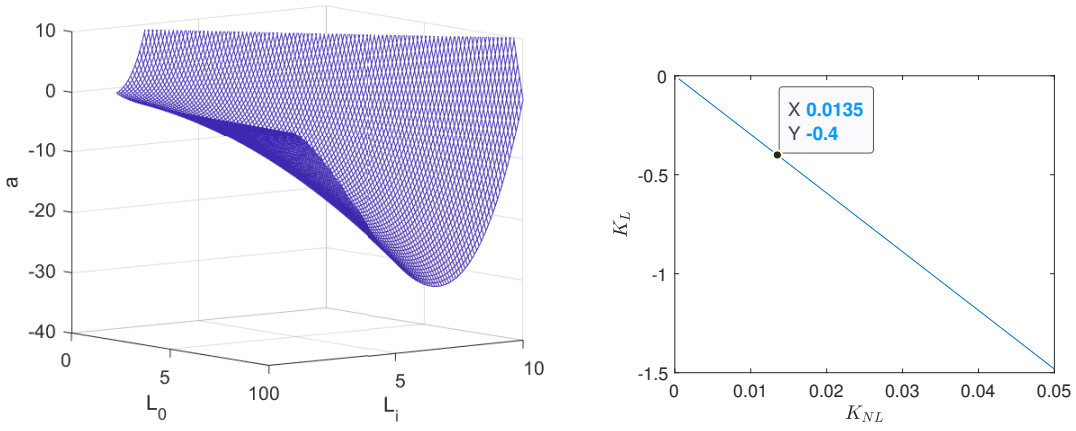

Figure 2.7: Influence of varying the lengths L_i and L_0 on the stiffness parameters of transverse spring.

Figure 2.8 shows the frequency response for both the linear and the system with different prestress conditions.

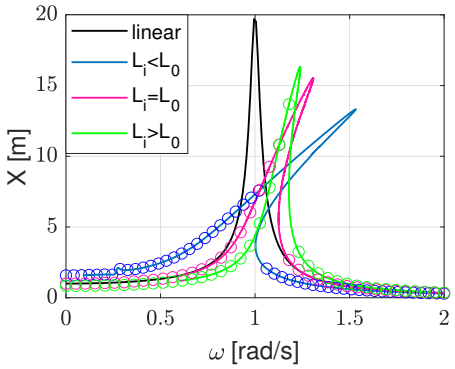

Figure 2.8: Frequency response under different prestress conditions. The black curve corresponds to the linear case, the blue curve to compression prestress, the magenta curve to the case without prestress, and the green curve to tension prestress. Solid lines are obtained using MatCont, while circles denote results from the fourth-order Runge–Kutta method.

Values used to generate the frequency response shown in figure 2.8 are presented in table 2.4.

Table 2.2: Parameters used in the frequency response shown in figure 2.8

Prestress	L_0 [m]	L_i [m]	K_L [N/m]	K_{NL} [N/m^3]
Compression	10	6.667	-0.4	0.01348
Whitout prestress	10	10	0	0.004
Tension	10	13.67	0.1985	0.0017

Analysing both the frequency response, shown in figure 2.8, and parameters, shown in table 2.4, it is evident that applying a compression prestress results in a leftward shift due to the negative value of K_L. This generates a lower equivalent linear stiffness compared to the system without the transversal spring. In the absence of prestress, the K_L term is zero, aligning the natural frequency with that one of the system without the transversal spring. Conversely, with a tension prestress, the positive value of K_L causes a rightward shift. In addition to these natural frequency shifts, a decrease in K_{NL} is observed when transitioning from compression to tension prestress. The reduction of this term decreases the influence of the transversal spring on the system, decreasing the

curvature or tilt of the curve.

Chapter 3

DYNAMICAL RESPONSE OF FINITE PERIODIC STRUCTURE

In this chapter, we examine the finite periodic structure, both linear and nonlinear, considering various prestress conditions. The analysis includes displacement transmissibilities (calculated using impedance method for linear system and fourth-order Runge-Kutta and continuation method for nonlinear system), bandgaps, phase planes and basins of attraction.

3.1 Response of Linear Periodic Structure

We use the method of mechanical impedance to solve the linear finite periodic structure and express the impedance $\mathbf{Z}$ in a general form as follows, where i denotes the imaginary unit:

$$\mathbf{Z}(i\omega) = -\omega^2\mathbf{M} + i\omega\mathbf{C} + \mathbf{K} \tag{3.1}$$

The linear finite periodic structure, obtained from the general model in figure 1.8 by

considering a finite number of cells and setting the transverse spring stiffness coefficient $k_a = 0$, can be solved using the following equation:

$$\mathbf{X} = [\mathbf{Z}(i\omega)]^{-1}\mathbf{F} \tag{3.2}$$

To conduct the bandgap analysis, the transmissibility is examined, representing the displacement ratio between the leftmost and rightmost blocks and is expressed as:

$$\mathbf{T} = \frac{X_1}{X_{2n+1}} \tag{3.3}$$

where the displacements $\mathbf{X}$ are obtained using the mechanical impedance method by equation 3.2.

As done in Carneiro *et al.* (2021), for a symmetric cell the characteristic frequencies of the bandgap and bandstop can be determined by equating the absolute value of transmissibility in equation 3.3 to one ($|T| = 1$). In this context, $T < 1$ corresponds to attenuation of the transmitted wave, whereas $T > 1$ corresponds to amplification. The frequencies ω_a and ω_b define the boundaries of the bandgap, that is, the frequency range where attenuation occurs. The frequency ω_c, in turn, marks the onset of the bandstop, beyond which attenuation is always present. These frequencies are given by the following equations:

$$\omega_a = \sqrt{\frac{k}{\mu m_1}}, \quad \omega_b = \sqrt{\frac{k}{m_1}}, \quad \omega_c = \sqrt{\frac{\mu k + k}{\mu m_1}} \tag{3.4}$$

In addition to equations related to transmissibility, it is also important to consider the natural frequencies of one cell, which are presented below:

$$\omega_1 = 0, \quad \omega_2 = \sqrt{\frac{k}{m_1}}, \quad \omega_3 = \sqrt{\frac{\mu k + k}{\mu m_1}} \tag{3.5}$$

It is worth noting that the expressions for ω_b and ω_c in equation 3.4 correspond exactly to the natural frequencies ω_2 and ω_3 obtained in equation 3.5. As a complementary illustration, figure 3.1 presents the vibration modes of the unit cell shown in figure 2.1(a) for three different mass ratios: $\mu = 0.5$, $\mu = 1$, and $\mu = 2$. Although not essential to the analysis, these mode shapes provide additional insight into the dynamic behaviour of the system.

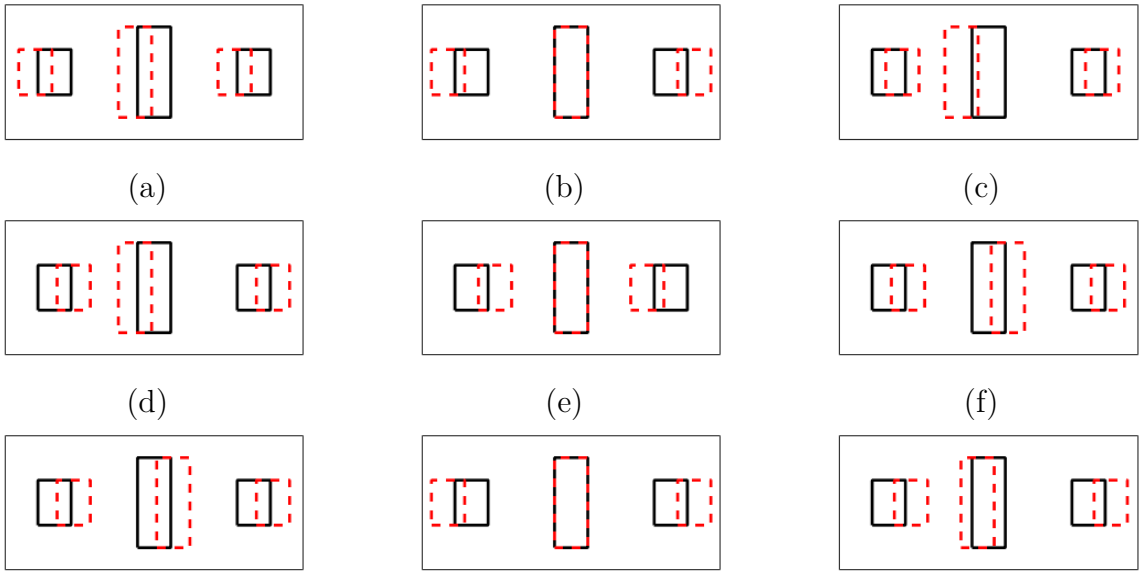

Figure 3.1: Modes of vibration, where (a)–(c) $\mu = 0.5$, (d)–(f) $\mu = 1$, and (g)–(i) $\mu = 2$.

3.1.1 Bandgap Analysis

Figure 3.2 shows transmissibility curves considering $\mu = 0.5$, $\mu = 1$, and $\mu = 2$, with vertical dashed lines indicating the frequencies in equation 3.4 and a horizontal dashed line indicating $|T| = 1$. The bandgap is bounded by ω_a and ω_b, depending on the mass ratio, while the bandstop is defined by ω_c. It can be observed that for the existence of

a bandgap, it is necessary for the mass ratio to be different from 1.

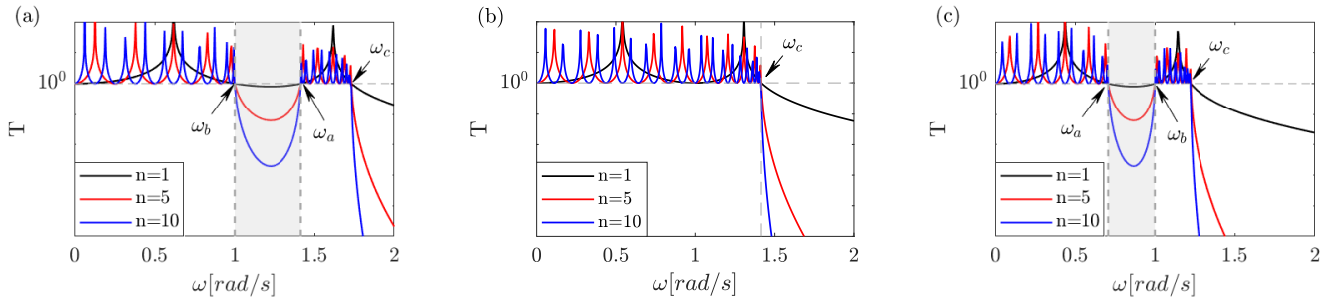

Figure 3.2: Transmissibility curves for linear periodic structures with (a) $\mu = 0.5$, (b) $\mu = 1$, and (c) $\mu = 2$, considering one, five, and ten unit cells. Vertical dashed lines indicate the theoretical bounds of the bandgap, as given by equation 3.4, and the horizontal dashed line represents $|T| = 1$.

This figure allows a detailed visualization of well-established phenomena in linear periodic structures by combining variations in mass ratio with different numbers of cells. Regardless of the number of cells in the finite structure, the limits of the attenuation region remain approximately fixed. These boundaries are defined by the dispersion relation of the infinite structure and closely related to the natural frequencies of the unit cell. Specifically, the expressions for ω_b and ω_c in equation 3.4 correspond exactly to the second and third natural frequencies ω_2 and ω_3 obtained in equation 3.5.

As the number of cells increases, the attenuation within the bandgap becomes more pronounced, although the bandgap region is already identifiable even in the case of a single cell. This indicates that the underlying attenuation mechanism is already present at the unit-cell level, but its effect is enhanced by the periodic repetition of the cell. As the number of cells increases to $N = 5$ and 10, the attenuation becomes significantly deeper. This behavior reflects the cumulative effect of periodicity, which amplifies destructive interference and improves wave filtering performance.

The mass ratio μ has a significant influence on the location of the bandgap. When $\mu = 1$, the structure is symmetric and no bandgap is formed, since the local resonators do not provide the asymmetry necessary to induce destructive interference. When $\mu = 0.5$, the bandgap shifts to higher frequencies, whereas for $\mu = 2$, it shifts to lower

frequencies. This behavior reflects the analytical dependence of ω_2 and ω_3 on the mass ratio. Furthermore, the edges of the bandgap observed in the transmissibility plots align with the natural frequencies of the unit cell, but the correspondence depends on μ: for $\mu = 0.5$, ω_2 marks the lower limit of the bandgap, and ω_3 its upper limit; for $\mu = 2$, this relationship is reversed.

In summary, the results in Figure 3.2 consolidate the classical understanding of linear periodic structures, highlighting how unit cell parameters (e.g., mass ratio) and the number of cells influence the formation and location of bandgaps. These linear mechanisms—rooted in symmetry breaking, local resonances, and interference effects - serve as a crucial reference for interpreting more complex phenomena. In the following section, these foundations will be used to explore how geometric nonlinearities affect the system's dynamic response.

3.2 Response of Nonlinear Periodic Structure

This section investigates the nonlinear periodic structure through transmissibility analysis, phase portraits, Poincaré sections, Lyapunov exponents, and basins of attraction, with transmissibility computed using both continuation via MatCont and the fourth-order Runge–Kutta method.

3.2.1 Continuation Method

To demonstrate the application of the continuation method using the MatCont toolbox in Matlab®, the procedure for analysing a single cell in the structure is presented below. This methodology can be extended to a periodic structure with n cells. The dynamical equations for the cell shown in figure 2.1(a) are obtained from Newton's second law as follows:

$$
\begin{aligned}
\ddot{x}_1 &= \frac{-c\dot{x}_1 + c\dot{x}_2 - kx_1 + kx_2}{m_1} \\
\ddot{x}_2 &= \frac{1}{2\mu m_1}\left(-2c\dot{x}_2 + c\dot{x}_3 - 2kx_2 + kx_3 - \frac{2k_a(L_i - L_0)x_2}{L_1} - \frac{L_0 k_a x_2^3}{L_i^3}\right) \\
\ddot{x}_3 &= \frac{1}{m_1}\left(c\dot{x}_2 - c\dot{x}_3 + kx_2 - kx_3 + F_0 cos(\omega t)\right)
\end{aligned} \tag{3.6}
$$

MatCont toolbox allows for the continuation of periodic solutions for first-order nonlinear autonomous equations. Initially, the following state variables are considered:

$$
y_1 = x_1, \quad y_2 = \dot{x}_1, \quad y_3 = x_2, \quad y_4 = \dot{x}_2, \quad y_5 = x_3, \quad y_6 = \dot{x}_3 \tag{3.7}
$$

Substituting equation 3.7 in equation 3.6, we have the following equations in the state-space:

$$
\begin{aligned}
\dot{y}_1 &= y_2 \\
\dot{y}_2 &= \frac{-cy_2 + cy_4 - ky_1 + ky_3}{m_1} \\
\dot{y}_3 &= y_4 \\
\dot{y}_4 &= \frac{1}{2\mu m_1}\left(-2cy_4 + cy_6 - 2ky_3 + ky_5 - \frac{2k_a(L_i - L_0)y_3}{L_1} - \frac{L_0 k_a y_3^3}{L_i^3}\right) \\
\dot{y}_5 &= y_6 \\
\dot{y}_6 &= \frac{1}{m_1}\left(cy_4 - cy_6 + ky_3 - ky_5 + F_0 cos(\omega t)\right)
\end{aligned} \tag{3.8}
$$

Equations 3.8 are initially non-autonomous and first-order. However, to utilise MatCont, it is necessary to convert them into autonomous equations. This conversion is achieved by applying the Hopf-normal form:

$$\dot{u} = -\omega v + u(1 - u^2 - v^2)$$
$$\dot{v} = \omega u + v(1 - u^2 - v^2) \tag{3.9}$$

Combining equations 3.8 and 3.9, we have the first order autonomous system for using numerical continuation:

$$\begin{aligned}
\dot{y}_1 &= y_2 \\
\dot{y}_2 &= \frac{-cy_2 + cy_4 - ky_1 + ky_3}{m_1} \\
\dot{y}_3 &= y_4 \\
\dot{y}_4 &= \frac{1}{2\mu m_1}\left(-2cy_4 + cy_6 - 2ky_3 + ky_5 - \frac{2k_a(L_i - L_0)y_3}{L_1} - \frac{L_0 k_a y_3^3}{L_i^3}\right) \\
\dot{y}_5 &= y_6 \\
\dot{y}_6 &= \frac{1}{m_1}\left(cy_4 - cy_6 + ky_3 - ky_5 + F_0 u\right) \\
\dot{u} &= -\omega v + u(1 - u^2 - v^2) \\
\dot{v} &= \omega u + v(1 - u^2 - v^2)
\end{aligned} \tag{3.10}$$

3.2.2 Dynamical Response Analysis

This section presents an analysis of nonlinear dynamical response of the periodic structure with five cells under different prestresses. The results are organised according to the applied axial pre-compression, no prestress, and pre-tension conditions. For each case, the system behaviour is investigated considering two distinct mass ratios ($\mu < 1$ and $\mu > 1$). The analysis includes Poincaré sections, Lyapunov exponents, and basins of attraction, providing both qualitative and quantitative insights into the system's stability and potential for complex nonlinear phenomena such as bifurcations and chaos.

The basins of attraction are computed by varying the initial conditions exclusively at the 11^{th} degree of freedom—corresponding to the rightmost mass where the external excitation is applied—in order to assess how perturbations in that region influence the global response of the structure.

The case $\mu = 1$ is not considered in the nonlinear analysis because the linear results show that no bandgap is present for this mass ratio, indicating the absence of any frequency range of wave attenuation in the corresponding linear system. For this reason, the nonlinear analysis focused solely on the cases $\mu = 0.5$ and $\mu = 2$.

To facilitate visual identification across the different transmissibility analyses, a consistent color scheme is adopted: black curves represent the linear case, blue is used for the compression prestress condition, magenta for the case without prestress, and green for tension prestress. In all figures, unstable solution branches are shown in red, regardless of the prestress condition.

It is important to note that the nonlinear curves could not be fully traced using the continuation method due to the "current step size too small" error, caused by the difficulty in achieving the steady-state necessary to complete the numerical method.

Compression Prestress

Figure 3.3 presents the transmissibility of the linear periodic structure in black, obtained through mechanical impedance method. The nonlinear responses under compression prestress are shown in blue and red, computed via continuation using Matcont. Blue indicates stable responses, while red denotes unstable ones. Blue circles indicate responses obtained through the fourth-order Runge-Kutta method, showing good agreement with the Matcont results.

For $\mu = 2$ a reduction in the bandgap width is observed, along with the emergence of instability within this region and it was not possible to complete the continuation curve at low frequencies. In contrast, for $\mu = 0.5$, instabilities appear at lower frequencies, while the bandgap is shifted to higher frequencies and its width increases due to a delayed

onset and reduced peak amplitude. These observations can be physically explained by the influence of geometric nonlinearity introduced by the compression prestress. This nonlinearity shifts the system's static equilibrium away from the origin, reduces the effective stiffness, and alters the wave propagation characteristics.

The reduction in the bandgap and the emergence of unstable branches are consistent with softening-type bifurcations. The mass ratio also plays a key role: for $\mu = 2$, the increased inertia at the degree of freedom where the force is applied amplifies dynamic effects and hinders convergence of the continuation method, especially at low frequencies. Conversely, for $\mu = 0.5$, the lower inertia makes the system more susceptible to harmonic excitation, leading to early onset of instability.

Furthermore, the Poincaré sections shown in figures 3.4 and 3.5 reveal that the dynamic equilibrium does not occur at the origin due to the displacement induced by the compressive prestress.

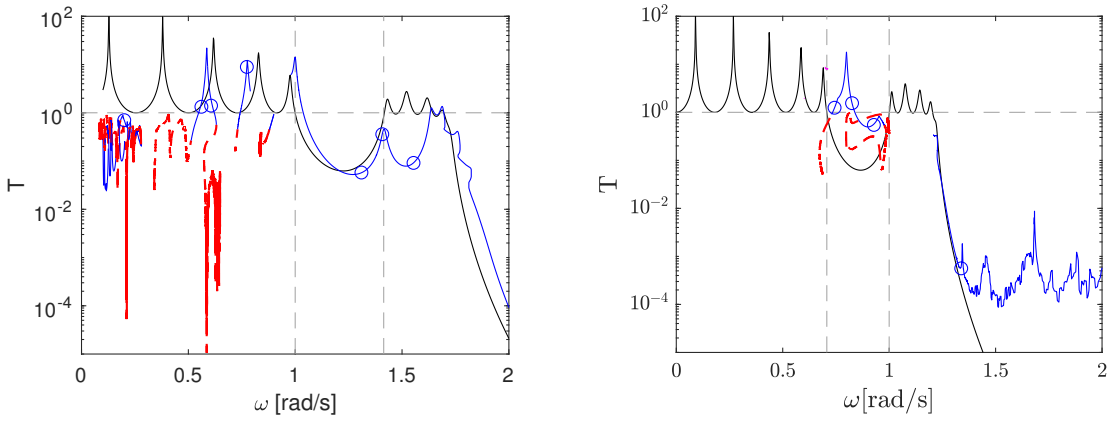

Figure 3.3: Transmissibility of nonlinear periodic structure under compression prestress. (a) Mass ratio $\mu = 0.5$; (b) Mass ratio $\mu = 2$. Black curve represents the linear analytical solution. Solid blue curve corresponds to the nonlinear stable branch computed via continuation (Matcont), while the dashed red curve indicates the unstable branch. Blue circles denote the transmissibility obtained through fourth-order Runge–Kutta method.

Figure 3.4(a) shows the transmissibility of the nonlinear periodic structure under compression prestress with $\mu = 0.5$. Vertical orange dashed lines indicate the excitation frequencies used in the basins of attraction: (b) $\omega = 0.3$ [rad/s], and (c) $\omega = 1.3$ [rad/s]. In (b), a mix of periodic (blue) and chaotic (red) responses is observed, demonstrating strong sensitivity to initial conditions and suggesting comparable probabilities of each regime. The interlaced nature of these solutions makes the system's long-term behaviour difficult to predict. Yellow circles mark the initial conditions used to compute the representative responses shown in (d)–(f). At $\omega = 1.3$ [rad/s], in (c), only periodic responses are observed, indicating a more regular dynamical regime at higher excitation frequencies.

Figure (d) presents a Poincaré section of a period-1 orbit from the dark blue region in (b), using $y_{11} = -8$ and $\dot{y}11 = 3.8$ as initial conditions. Panels (e) and (f) correspond to a chaotic response from the red region in (b), obtained with $\dot{y}11 = 1.6$ and all other initial conditions set to zero. Specifically, (e) shows the Poincaré section and (f) the corresponding Lyapunov exponent, where the positive value confirms the chaotic nature of the trajectory. The 11^{th} degree of freedom, where the excitation is applied, corresponds to the rightmost mass. The periodic solution exhibits a noticeable shift due to the compression prestress effect and these results emphasize that, under compression, the nonlinear structure exhibits highly sensitive and nonlinear dynamics at low frequencies.

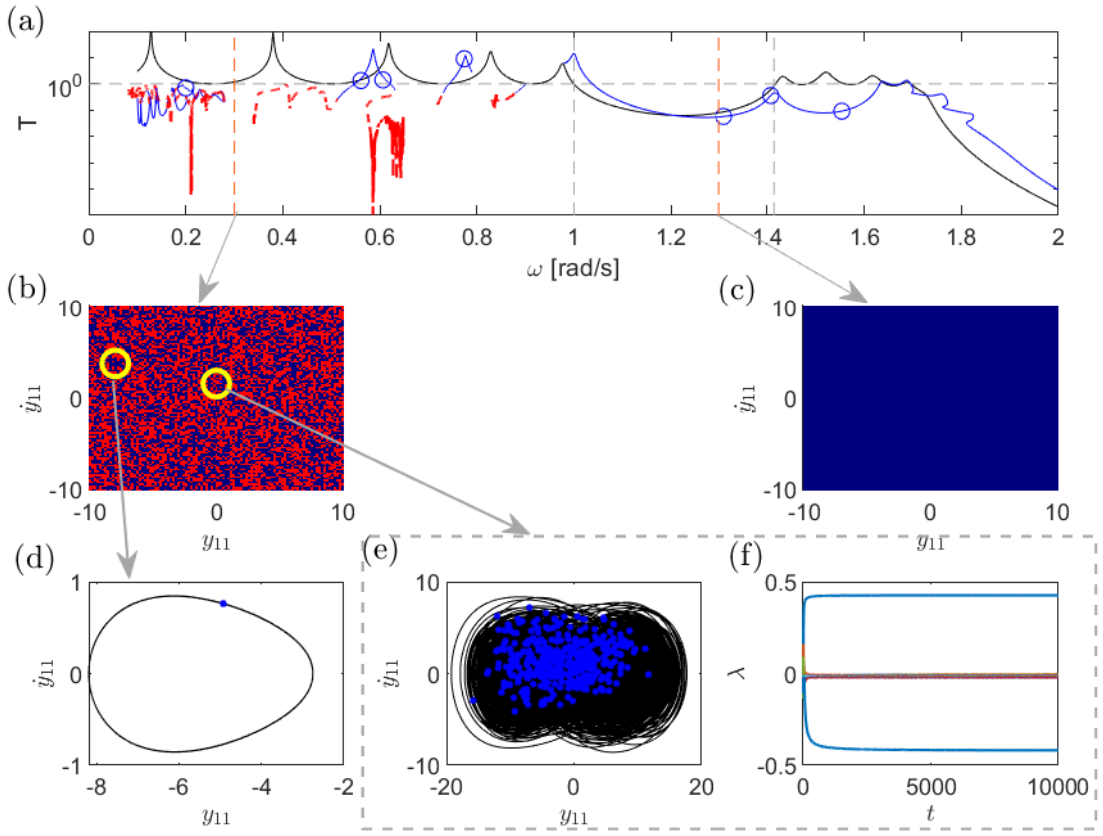

Figure 3.4: (a) Transmissibility of the nonlinear periodic structure under compression prestress with $\mu = 0.5$. The black curve shows the linear analytical solution; the solid blue and dashed red curves represent the stable and unstable nonlinear branches, respectively. Blue circles denote results from the fourth-order Runge–Kutta method. (b)–(c) Basins of attraction for excitation frequencies (b) $\omega = 0.3$ and (c) $\omega = 1.3$ [rad/s]. Yellow circles mark initial conditions used to illustrate the system responses. (d) Poincaré section for a period-1 response (dark blue region in (b)), obtained with $y_{11} = -8$ and $\dot{y}_{11} = 3.8$. (e)–(f) Poincaré section and Lyapunov exponent for a chaotic response (red region in (b)), using null initial conditions except for $\dot{y}_{11} = 1.6$. The 11^{th} degree of freedom corresponds to the rightmost mass, where the external excitation is applied. Colours in the basins represent different long-term behaviours based on spectral classification: — period-1 (low amplitude), — period-1 (high amplitude), — quasi-periodic, — chaotic.

Figure 3.5(a) presents the transmissibility of the nonlinear periodic structure under compression prestress with $\mu = 2$. Vertical orange dashed lines indicate the excitation frequencies used in the basin analyses: (b) $\omega = 0.2$, (c) $\omega = 0.3$, and (d) $\omega = 1.1$ [rad/s]. At $\omega = 0.2$, only quasi-periodic responses are observed (green), while for $\omega = 0.3$ and 1.1, the system exhibits purely chaotic responses (red). These results reflect strong nonlinearity and sensitivity to initial conditions, while also suggesting that the dominance of a single regime can make the system's long-term behaviour more predictable. Additionally, they reveal how the mass ratio influences the dynamics: a higher mass ratio increases the system's inertia and alters the balance between kinetic and potential energies, favouring complex responses such as quasi-periodicity and chaos.

Figure (e) shows a Poincaré section for the quasi-periodic regime at $\omega = 0.2$ [rad/s], obtained with null initial conditions. The shift in the equilibrium position due to compression prestress is also visible. Figures (f) and (g) correspond to a chaotic response at $\omega = 0.3$ [rad/s], both obtained with all initial conditions set to zero. The irregular pattern in (f) and the positive Lyapunov exponent in (g) confirm the chaotic nature of the motion.

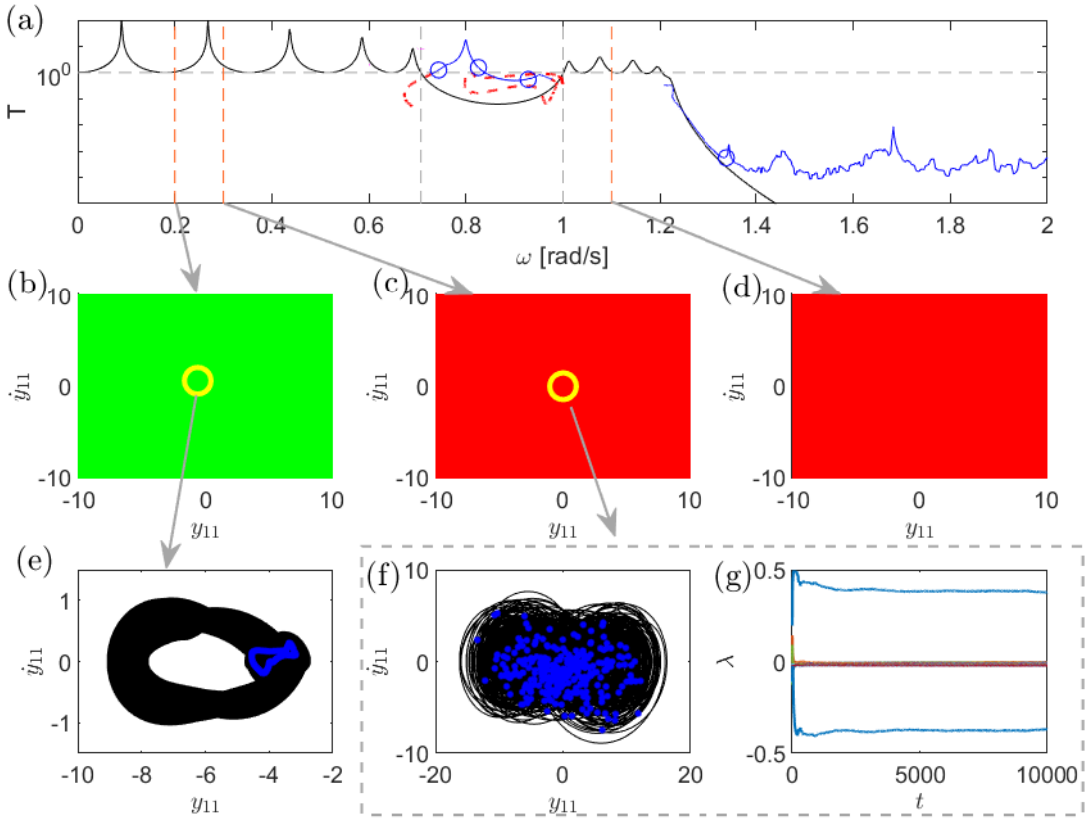

Figure 3.5: (a) Transmissibility of the nonlinear periodic structure under compression prestress with $\mu = 2$. The black curve shows the linear analytical solution; the solid blue and dashed red curves represent the stable and unstable nonlinear branches, respectively. Blue circles denote results from the fourth-order Runge–Kutta method. (b)–(d) Basins of attraction for excitation frequencies (b) $\omega = 0.2$, (c) $\omega = 0.3$ and (d) $\omega = 1.1$ [rad/s]. Yellow circles mark initial conditions used to illustrate the system responses. (e) Poincaré section for a quasi-periodic response, obtained with null initial conditions. (f)–(g) Poincaré section and Lyapunov exponent for a chaotic response, obtained with null initial conditions. The 11^{th} degree of freedom corresponds to the rightmost mass, where the external excitation is applied. Colours in the basins represent different long-term behaviours based on spectral classification: — period-1 (low amplitude), — period-1 (high amplitude), — quasi-periodic, — chaotic.

The comparison between $\mu = 0.5$ and $\mu = 2$ highlights the influence of mass ratio on the system's nonlinear dynamics. For $\mu = 0.5$, low-frequency excitation leads to a coexistence of periodic and chaotic regimes attractors, with strong sensitivity to initial conditions. In contrast, for $\mu = 2$, the responses become predominantly quasi-periodic or chaotic, depending on the excitation frequency, with no low-amplitude periodic regimes observed. These results suggest that increasing the mass ratio enhances inertial effects, intensifies nonlinearity behaviour, and promotes the emergence of more complex behaviours, such as chaos and quasi-periodicity, across a broader frequency range.

No Prestress

Figure 3.6 shows the transmissibility of the linear periodic structure (black curve) and the nonlinear response without prestress (magenta and red), computed via continuation using Matcont. Stable branches are shown in magenta, while unstable ones are in red. Magenta circles indicate responses obtained through the fourth-order Runge-Kutta method, showing good agreement with the Matcont results.

A noticeable reduction in the bandgap region is observed in the nonlinear system, along with low-frequency attenuation. Unstable responses are primarily concentrated at low frequencies for both mass ratios $\mu = 0.5$ and $\mu = 2$. In both cases, the bandstop frequency shifts slightly to the left, indicating a decrease in the effective cutoff frequency. This shift and the emergence of instabilities are likely due to the nonlinear stiffness terms, which alter the effective dynamic properties of the system.

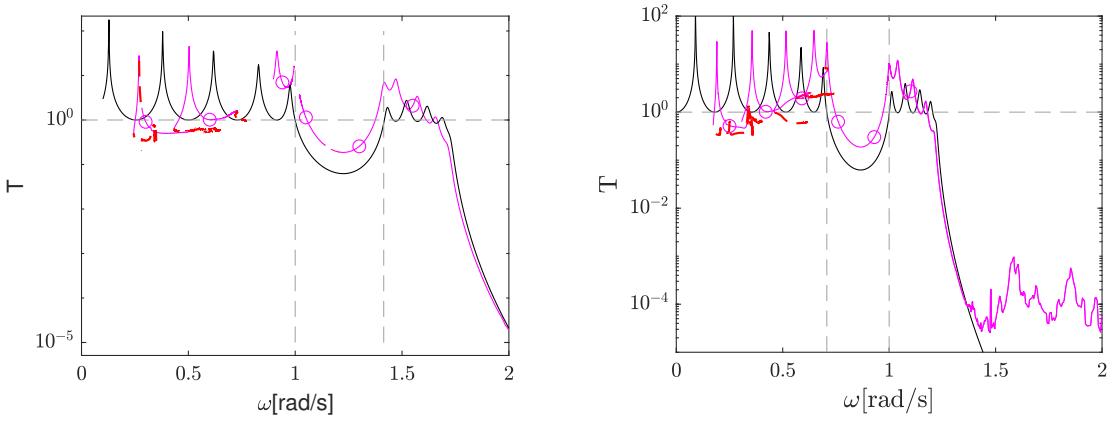

Figure 3.6: Transmissibility of nonlinear periodic structure whithout prestress. (a) Mass ratio $\mu = 0.5$; (b) Mass ratio $\mu = 2$. Black curve represents the linear analytical solution. Solid magenta curve corresponds to the nonlinear stable branch computed via continuation (Matcont), while the dashed red curve indicates the unstable branch. Magenta circles denote the transmissibility obtained through fourth-order Runge–Kutta method.

Figure 3.7(a) presents the transmissibility of the nonlinear periodic structure without prestress for $\mu = 0.5$. Vertical orange dashed lines indicate the excitation frequencies used in the basin analyses: (b) $\omega = 0.2$, (c) $\omega = 0.3$, (d) $\omega = 0.45$, and (e) $\omega = 0.71$ [rad/s]. Yellow circles mark the initial conditions selected to illustrate the corresponding system responses. The results reveal a predominance of periodic and quasi-periodic behaviours across most frequencies. However, chaotic dynamics emerge even at relatively low frequencies, such as $\omega = 0.45$ [rad/s], underscoring the system's sensitivity to initial conditions and the potential for complex dynamics even in the absence of prestress.

Figure (f) shows a quasi-periodic response based on the Poincaré section, obtained using $y_{11} = 1$ and $\dot{y}_{11} = -0.2$, with all other states set to zero. A period-1 orbit obtained from null initial conditions is shown in (g), while another period-1 response with significantly higher amplitude appears in (h), using $y_{11} = -0.6$ and $\dot{y}_{11} = 8.8$. Although both (g) and (h) exhibit periodic behaviour, their amplitudes differ considerably. Unlike in the compression prestress case, all responses here oscillate around the zero equilibrium, reflecting the absence of static displacement. The variations in response types under different initial conditions highlight the structure's sensitivity and the strong influence of nonlinearities on its dynamic behaviour.

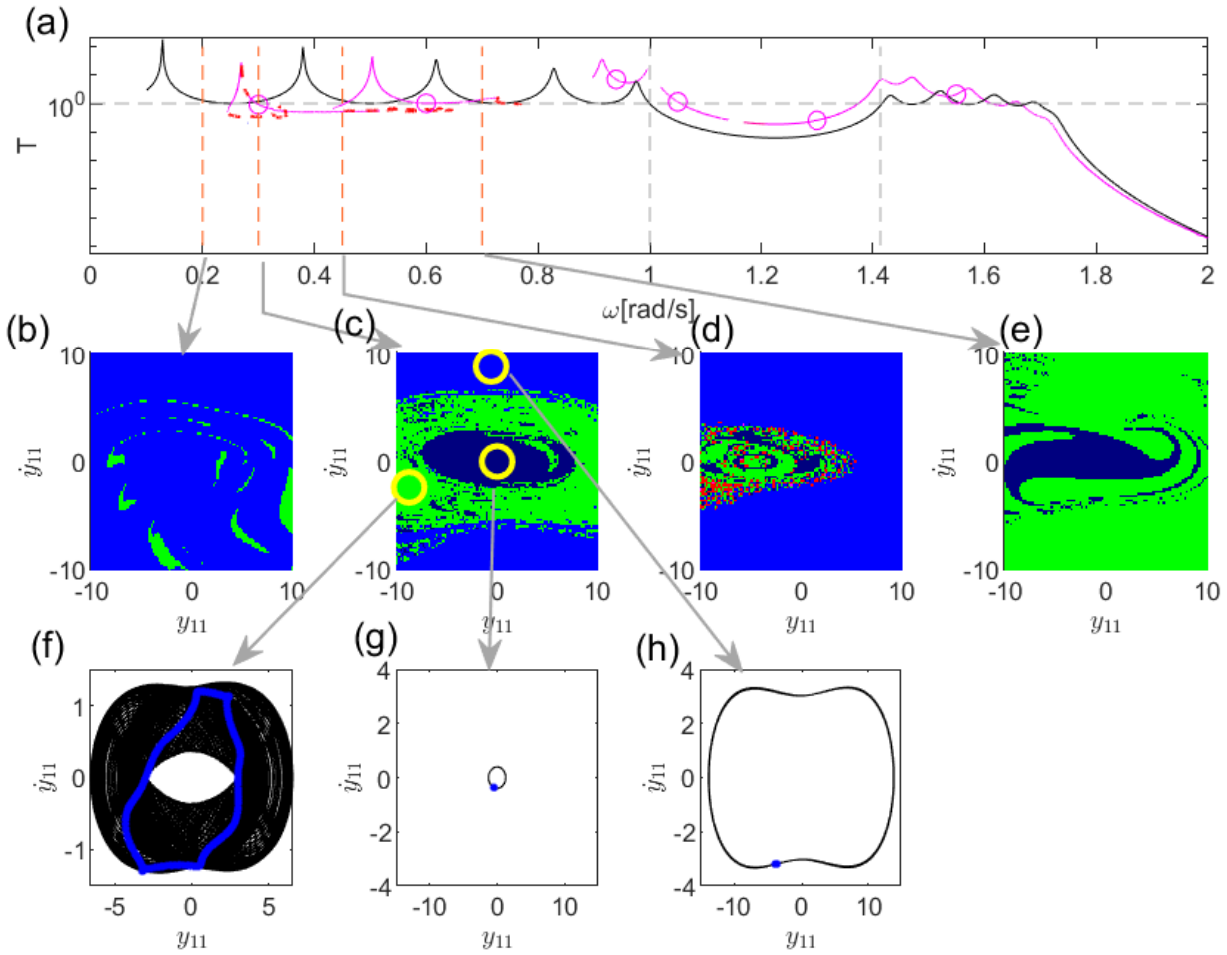

Figure 3.7: (a) Transmissibility of the nonlinear periodic structure without prestress with $\mu = 0.5$. The black curve shows the linear analytical solution; the solid magenta and dashed red curves represent the stable and unstable nonlinear branches, respectively. Magenta circles denote results from the fourth-order Runge–Kutta method. (b)–(e) Basins of attraction for excitation frequencies (b) $\omega = 0.2$, (c) $\omega = 0.3$, (d) $\omega = 0.45$ and (e) $\omega = 0.71$ [rad/s]. Yellow circles mark initial conditions used to illustrate the system responses. (f) Poincaré section (green region in (c)), using initial conditions $y_{11} = -8.8$ and $\dot{y}_{11} = -2.4$; (g) periodic response with low amplitude (dark blue region in (c)), corresponding to initial conditions set to zero for all degrees of freedom; (h) periodic response with high amplitude (light blue region in (c)), using initial conditions $y_{11} = -0.6$ and $\dot{y}_{11} = 8.8$. The 11^{th} degree of freedom corresponds to the rightmost mass, where the external excitation is applied. Colours in the basins represent different long-term behaviours based on spectral classification: — period-1 (low amplitude), — period-1 (high amplitude), — quasi-periodic, — chaotic.

Figure 3.8(a) presents the transmissibility of the nonlinear periodic structure without prestress for $\mu = 2$. Vertical orange dashed lines indicate the excitation frequencies used in the basin analyses: (b) $\omega = 0.2$, (c) $\omega = 0.71$, and (d) $\omega = 1.1$ [rad/s]. Yellow circles highlight the initial conditions selected to illustrate the corresponding system responses. The results indicate a predominance of periodic and quasi-periodic behaviours across most frequencies, with chaotic responses already emerging at low excitation levels, such as $\omega = 0.2$ [rad/s]. These observations reflect the system's sensitivity to initial conditions and how nonlinear effects can induce complex dynamics even in the absence of prestress.

Figure (h) shows a period-1 orbit (Poincaré section) obtained from initial conditions $y_{11} = -0.6$, $\dot{y}_{11} = 1.2$ (blue region in (b)), while (g) displays a quasi-periodic trajectory from initial conditions $y_{11} = 1$, $\dot{y}_{11} = -0.2$ (green region in (b)). Figures (e) and (f) correspond to a chaotic response from the red region in (b), obtained using $y_{11} = -8.8$ and $\dot{y}_{11} = -7.6$. Specifically, (e) shows the Poincaré section and (f) the Lyapunov exponent, whose positive value confirms the chaotic nature of the trajectory. As in the previous case without prestress, all solutions oscillate around the zero equilibrium. The variations in response types under different initial conditions highlight the structure's sensitivity and the strong influence of nonlinearities on its dynamic behaviour.

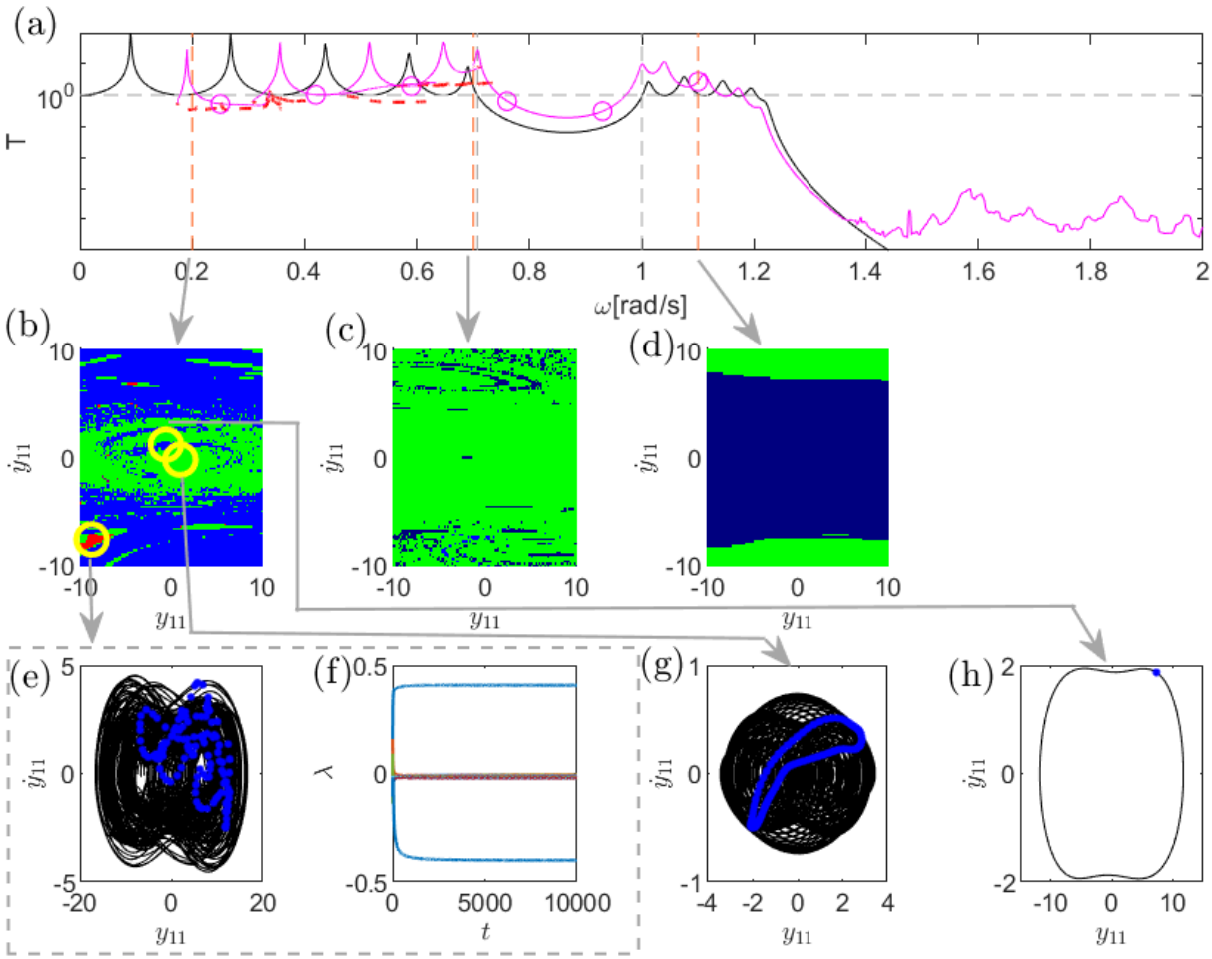

Figure 3.8: (a) Transmissibility of the nonlinear periodic structure without prestress with $\mu = 2$. The black curve shows the linear analytical solution; the solid magenta and dashed red curves represent the stable and unstable nonlinear branches, respectively. Magenta circles denote results from the fourth-order Runge–Kutta method. (b)–(d) Basins of attraction for excitation frequencies (b) $\omega = 0.2$, (c) $\omega = 0.71$ and (d) $\omega = 1.1$ [rad/s]. Yellow circles mark initial conditions used to illustrate the system responses. (h) Poincaré section for a periodic response (light blue region in (b)), using initial conditions $y_{11} = -0.6$ and $\dot{y}_{11} = 1.2$; (g) Poincaré section for a quasi-periodic response (green region in (b)), with $y_{11} = 1$ and $\dot{y}_{11} = -0.2$; (e) Poincaré section, and (f) Lyapunov exponent for a chaotic regime (red region in (b)), with initial conditions $y_{11} = -8.8$ and $\dot{y}_{11} = -7.6$. The 11^{th} degree of freedom corresponds to the rightmost mass, where the external excitation is applied. Colours in the basins represent different long-term behaviours based on spectral classification: — period-1 (low amplitude), — period-1 (high amplitude), — quasi-periodic, — chaotic.

A comparison between the responses for $\mu = 0.5$ and $\mu = 2$ in the absence of prestress reveals notable differences in the system's dynamic behaviour. For both cases, the system exhibits a mix of periodic, quasi-periodic, and chaotic regimes, indicating that even without prestress, the nonlinearities are sufficient to generate complex dynamics. However, the emergence of chaos occurs at different frequency ranges and under different initial conditions depending on the mass ratio.

For $\mu = 0.5$, chaotic behaviour appears at intermediate frequencies (e.g., $\omega = 0.45$ [rad/s]), while the response is mostly periodic or quasi-periodic at lower and higher frequencies. In contrast, for $\mu = 2$, chaos is observed even at $\omega = 0.2$ [rad/s], suggesting that the increased inertia promotes earlier onset of irregular dynamics. These findings highlight how the mass ratio influences not only the type of response but also the frequency thresholds at which transitions between regimes occur. In both cases, all responses oscillate around the zero equilibrium, emphasizing the role of prestress in shifting the static response baseline.

Tension Prestress

Figure 3.9 shows the transmissibility of the linear periodic structure (black curve) and the nonlinear response with tension prestress (green and red), computed via continuation using Matcont. Stable branches are shown in green, while unstable ones are in red. Green circles indicate responses obtained through the fourth-order Runge-Kutta method, showing good agreement with the Matcont results.

For the mass ratio $\mu = 0.5$, both the lower and upper bounds of the bandgap and bandstop shifted to higher frequencies. This behaviour is likely due to the tension prestress increasing the effective stiffness of the system, resulting in a hardening-type nonlinearity. At low frequencies, the continuation method failed to capture the nonlinear response, possibly due to complex dynamics induced by the mass ratio.

In contrast, for $\mu = 2$, the bandgap region narrows and the bandstop shifts to lower frequencies. In this case, the continuation method successfully traced the response even

at low frequencies, where attenuation is observed. The increase in mass leads to higher inertia, which may contribute to smoother dynamics and more accessible numerical tracking in this frequency range.

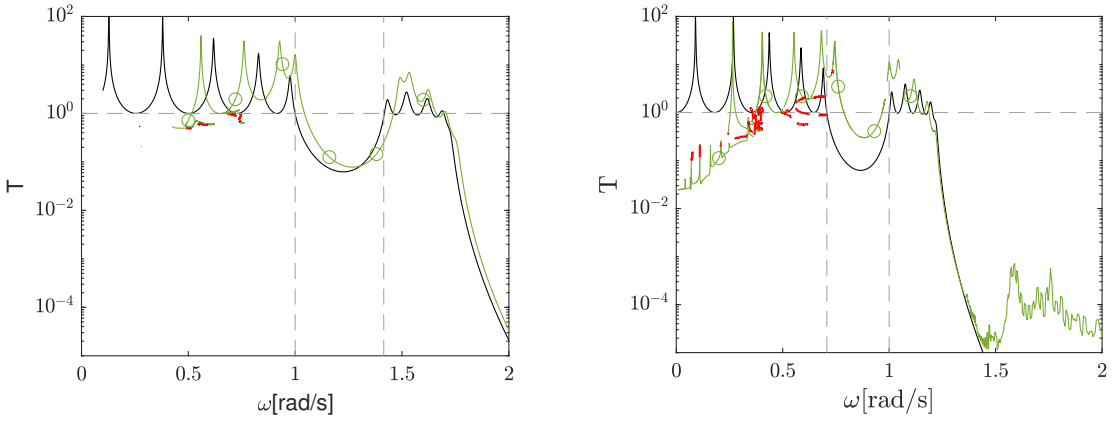

Figure 3.9: Transmissibility of nonlinear periodic structure whithout prestress. (a) Mass ratio $\mu = 0.5$; (b) Mass ratio $\mu = 2$. Black curve represents the linear analytical solution. Solid green curve corresponds to the nonlinear stable branch computed via continuation (Matcont), while the dashed red curve indicates the unstable branch. Green circles denote the transmissibility obtained through fourth-order Runge–Kutta method.

Figure 3.10(a) presents the transmissibility of the nonlinear periodic structure under tension prestress for $\mu = 0.5$. Vertical orange dashed lines indicate the excitation frequencies used in the basin analyses: (b) $\omega = 0.3$, and (c) $\omega = 1.1$ [rad/s]. Yellow circles highlight the initial conditions selected to illustrate the corresponding system responses. Figures (d) and (e) show the corresponding Poincaré sections for (b) and (c), respectively, obtained using null initial conditions. Both responses exhibit period-1 behaviour with different amplitudes and equilibrium centred around zero, in contrast to the compression case, where the equilibrium was shifted away from zero due to the applied prestress.

The centred equilibrium and regular trajectories suggest that tension prestress increases the effective stiffness of the structure, promoting a hardening-type behaviour. As a result, the system exhibits a more linear-like and predictable dynamic response, especially in the low-amplitude regime, in contrast to the irregular and shifted responses induced by compressive prestress.

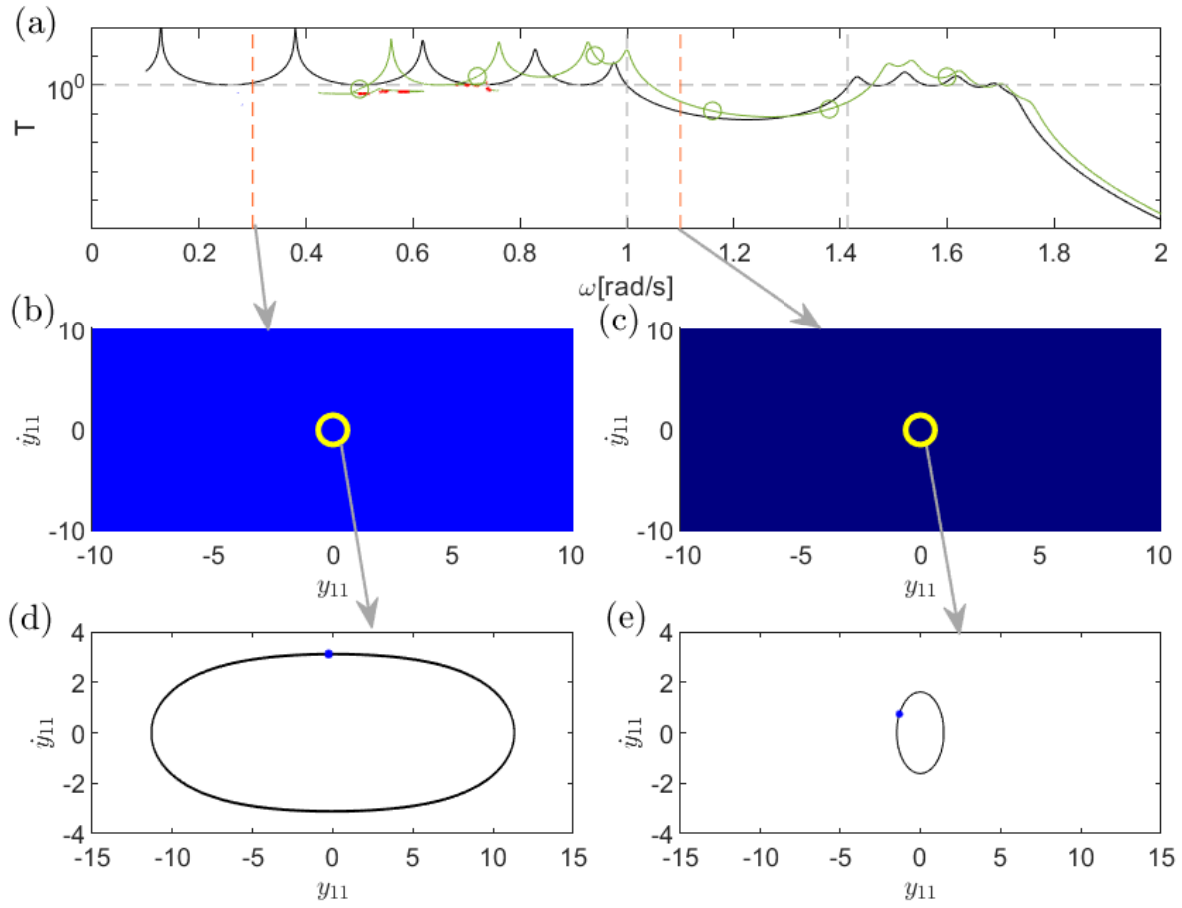

Figure 3.10: (a) Transmissibility of the nonlinear periodic structure under tension pre-stress with $\mu = 0.5$. The black curve shows the linear analytical solution; the solid green and dashed red curves represent the stable and unstable nonlinear branches, respectively. Green circles denote results from the fourth-order Runge–Kutta method. (b)–(c) Basins of attraction for excitation frequencies (b) $\omega = 0.3$, (c) $\omega = 1.1$ [rad/s]. Yellow circles mark initial conditions used to illustrate the system responses. (e) and (e) show the corresponding Poincaré sections for cases (b) and (c), respectively, using null initial conditions. The 11^{th} degree of freedom corresponds to the rightmost mass, where the external excitation is applied. Colours in the basins represent different long-term behaviours based on spectral classification: — period-1 (low amplitude), — period-1 (high amplitude), — quasi-periodic, — chaotic.

Figure 3.11(a) presents the transmissibility of the nonlinear periodic structure under tension prestress for $\mu = 2$. Vertical orange dashed lines indicate the excitation frequencies used in the basin analyses: (b) $\omega = 0.3$, and (c) $\omega = 0.71$ [rad/s]. Yellow circles highlight the initial conditions selected to illustrate the corresponding system responses. Figures (d) and (e) show the corresponding Poincaré sections for (b) and (c), respectively, obtained using null initial conditions. Both responses exhibit period-1 behaviour with different amplitudes and equilibrium centred around zero, in contrast to the compression case, where the equilibrium was shifted away from zero due to the applied prestress.

These results reinforce the trend observed for $\mu = 0.5$: tension prestress increases the effective stiffness and promotes a more regular, linear-like response. Even with a higher mass ratio, the system maintains predictable, low-complexity dynamics across the evaluated frequency range, with no indication of quasi-periodic or chaotic behaviour.

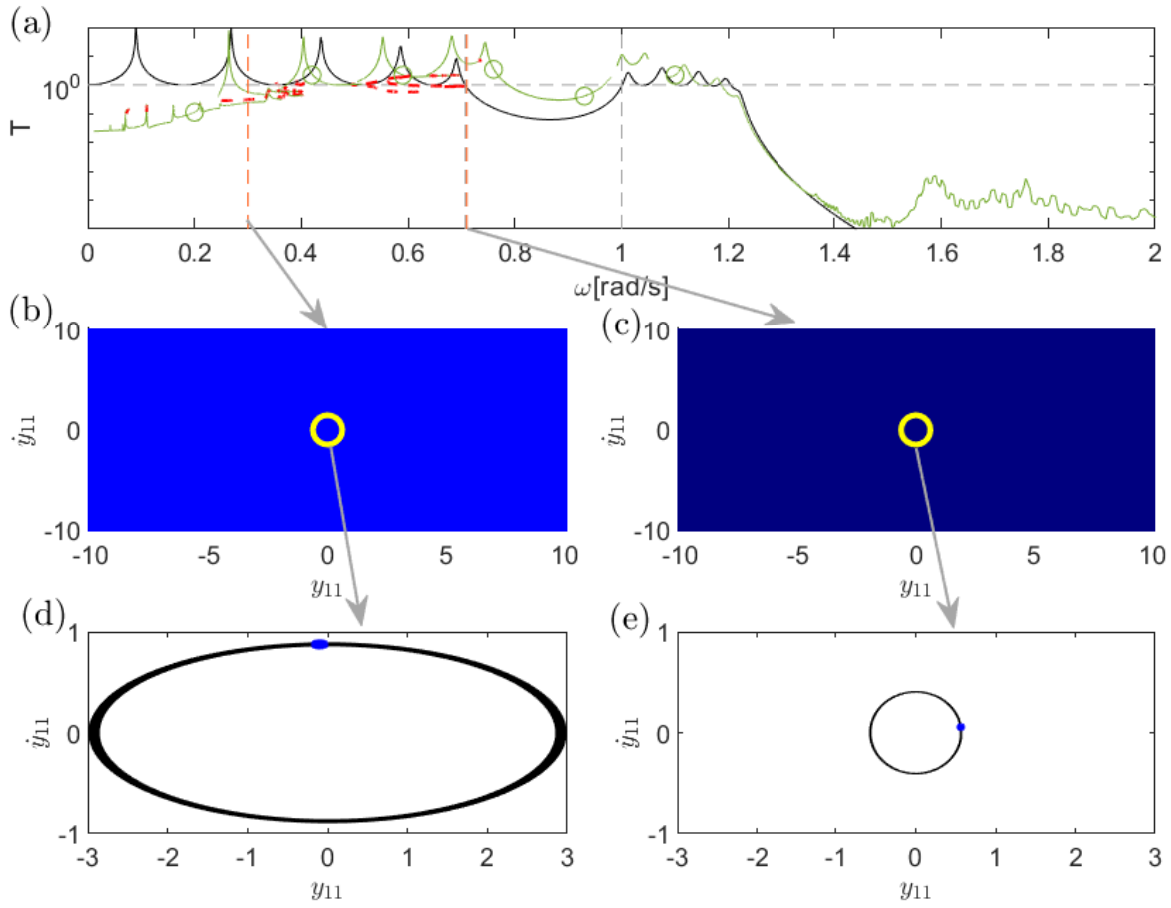

Figure 3.11: (a) Transmissibility of the nonlinear periodic structure under tension pre-stress with $\mu = 2$. The black curve shows the linear analytical solution; the solid green and dashed red curves represent the stable and unstable nonlinear branches, respectively. Green circles denote results from the fourth-order Runge–Kutta method. (b)–(c) Basins of attraction for excitation frequencies (b) $\omega = 0.3$, (c) $\omega = 0.71$ [rad/s]. Yellow circles mark initial conditions used to illustrate the system responses. (e) and (e) show the corresponding Poincaré sections for cases (b) and (c), respectively, using null initial conditions. The 11^{th} degree of freedom corresponds to the rightmost mass, where the external excitation is applied. Colours in the basins represent different long-term behaviours based on spectral classification: — period-1 (low amplitude), — period-1 (high amplitude), — quasi-periodic, — chaotic.

For both mass ratios, $\mu = 0.5$ and $\mu = 2$, the Poincaré sections reveal a reduction in phase-plane amplitude as the excitation frequency increases. This behaviour indicates that higher excitation frequencies tend to suppress the system's vibrational response, consistent with a hardening-type nonlinearity, where the effective stiffness increases with amplitude, reducing energy transmission at higher frequencies.

Comparison Between Prestress Conditions

This subsection provides a comparative analysis of the dynamic responses observed under different prestress conditions and mass ratios, aiming to highlight how compression, tension, and no prestress influence the nonlinear behaviour of the periodic structure.

This comparison highlights the crucial role these parameters play in the nonlinear dynamic response of the periodic structure. Without prestress, the system exhibits a variety of behaviours, including periodic, quasi-periodic, and even chaotic regimes, particularly within intermediate frequency ranges. The presence of chaos in the absence of prestress indicates that geometric nonlinearity alone is sufficient to induce complex responses, with sensitivity to initial conditions being an intrinsic feature of the system.

Under compression prestress, the response becomes even more sensitive, with the coexistence of multiple attractors and more prominent chaotic regions. Compression shifts the structure's static equilibrium, promoting instabilities and increasing the irregularity of the trajectories, especially for $\mu = 0.5$. For $\mu = 2$, quasi-periodic and chaotic behaviours dominate across a broader frequency range, suggesting that a higher mass ratio amplifies nonlinear effects and leads to earlier onset of complex dynamics.

In contrast, tension prestress results in more regular responses centred around the zero equilibrium, regardless of the mass ratio. For both $\mu = 0.5$ and $\mu = 2$, the system exhibits purely periodic responses with stable and predictable trajectories. This behaviour suggests that tension acts as an additional stiffness mechanism, inducing hardening-type dynamics that inhibit bifurcations and reduce sensitivity to initial conditions.

These findings demonstrate that the combination of prestress and mass ratio can

be strategically employed as a passive control mechanism to regulate the degree of nonlinear behaviour and the predictability of the system's dynamic response, depending on whether stability or complexity is desired in a given application.

Chapter 4

DYNAMICAL RESPONSE OF INFINITE PERIODIC STRUCTURE

In this chapter, we investigate the dynamic behaviour of infinite periodic structures, considering both linear and nonlinear formulations under different prestress conditions. The analysis relies on the dispersion relation, which characterizes wave propagation and identifies bandgap regions intrinsic to the periodic medium.

Studying the infinite structure provides fundamental insights into the underlying wave mechanics without the influence of boundary effects, serving as a theoretical reference for interpreting the results obtained in Chapter 3. Finally, a comparison between finite and infinite configurations is presented to highlight how edge conditions, nonlinear behaviour, and mass distribution affect wave attenuation and dynamic response.

4.1 Dispersion Relation of Linear Periodic Structure

The dispersion relation is obtained using a perturbation approach, following the methodology presented in (NARISETTI; LEAMY; RUZZENE, 2010). To assess the influence of the number of degrees of freedom in the unit cell, two configurations are analysed: a structure with two degrees of freedom and another with three, as illustrated in Figures 2.2(a) and 2.2(b). This comparison helps determine whether a more complex unit cell significantly alters the wave propagation characteristics.

4.1.1 Dispersion Relation Considering Three Degree-of-Freedom

Dynamical equations for the structure shown in figure 2.2(a) (without considering the transverse spring) are shown below:

$$\begin{aligned} 2m_1\ddot{u}_{j,1} + 2ku_{j,1} - ku_{j-1,2} - ku_{j,2} &= 0 \\ 2m_2\ddot{u}_{j,2} + 2ku_{j,2} - ku_{j,1} - ku_{j,3} &= 0 \\ 2m_1\ddot{u}_{j,3} + 2ku_{j,3} - ku_{j,2} - ku_{j+1,2} &= 0 \end{aligned} \tag{4.1}$$

By multiplying equation 4.1 by $\frac{1}{m_1\omega_n^2}$ and considering nondimensional time $\tau = \omega t$, linear natural frequency $\omega_n = \sqrt{k/m_1}$ and nondimensional frequency $\bar{\omega} = \omega/\omega_n$, the following equation in matrix form is obtained:

$$2\bar{\omega}^2 \begin{bmatrix} 1 & 0 & 0 \\ 0 & \mu & 0 \\ 0 & 0 & 1 \end{bmatrix} \begin{bmatrix} d^2u_{j,1}/d\tau^2 \\ d^2u_{j,2}/d\tau^2 \\ d^2u_{j,3}/d\tau^2 \end{bmatrix} + \begin{bmatrix} 2 & -1 & 0 \\ -1 & 2 & -1 \\ 0 & -1 & 2 \end{bmatrix} \begin{bmatrix} u_{j,1} \\ u_{j,2} \\ u_{j,3} \end{bmatrix} + \begin{bmatrix} -u_{j-1,2} \\ 0 \\ -u_{j+1,2} \end{bmatrix} = \begin{bmatrix} 0 \\ 0 \\ 0 \end{bmatrix} \tag{4.2}$$

To solve the system, the asymptotic expansion shown below is used:

$$u_j = u_j^{(0)}, \quad \omega = \omega_0 \tag{4.3}$$

By substituting equation 4.3 into equation 4.2, it is obtained:

$$2\bar{\omega}_0^2 \begin{bmatrix} 1 & 0 & 0 \\ 0 & \mu & 0 \\ 0 & 0 & 1 \end{bmatrix} \begin{bmatrix} d^2u_{j,1}^{(0)}/d\tau^2 \\ d^2u_{j,2}^{(0)}/d\tau^2 \\ d^2u_{j,3}^{(0)}/d\tau^2 \end{bmatrix} + \begin{bmatrix} 2 & -1 & 0 \\ -1 & 2 & -1 \\ 0 & -1 & 2 \end{bmatrix} \begin{bmatrix} u_{j,1}^{(0)} \\ u_{j,2}^{(0)} \\ u_{j,3}^{(0)} \end{bmatrix} + \begin{bmatrix} -u_{j-1,2}^{(0)} \\ 0 \\ -u_{j+1,2}^{(0)} \end{bmatrix} = \begin{bmatrix} 0 \\ 0 \\ 0 \end{bmatrix} \tag{4.4}$$

To solve the system, the following solutions are used:

$$\begin{bmatrix} u_{j,1}^{(0)} \\ u_{j,2}^{(0)} \\ u_{j,3}^{(0)} \end{bmatrix} = \begin{bmatrix} (A_1^{(0)}/2)e^{i\kappa a(2j-1)} \\ (A_2^{(0)}/2)e^{i\kappa a(2j)} \\ (A_3^{(0)}/2)e^{i\kappa a(2j+1)} \end{bmatrix} e^{i\tau} + cc$$
$$\begin{bmatrix} u_{j\pm1,1}^{(0)} \\ u_{j\pm1,2}^{(0)} \end{bmatrix} = \begin{bmatrix} (A_1^{(0)}/2)e^{i\kappa a(2(j\pm1)-1)} \\ (A_2^{(0)}/2)e^{i\kappa a(2(j\pm1))} \end{bmatrix} e^{i\tau} + cc \tag{4.5}$$

By substituting equation 4.5 into equation 4.4, two branches for the linear dispersion are obtained:

$$\bar{\omega}_0^{opt} = \sqrt{\frac{\sqrt{\mu^2 + (4\cos(a\kappa)^2 - 2)\mu + 1} + \mu + 1}{2\mu}}$$
$$\bar{\omega}_0^{aco} = \sqrt{\frac{-\sqrt{\mu^2 + (4\cos(a\kappa)^2 - 2)\mu + 1} + \mu + 1}{2\mu}} \tag{4.6}$$

By Substituting each solution of equation 4.6 into equation 4.4, it is possible to obtain the amplitude ratio for each mode, as shown below:

$$\eta_{opt} = \frac{A_2^{(0)}}{A_1^{(0)}} = \frac{2\mu - \sqrt{\mu^2 + (4\cos(a\kappa)^2 - 2)\mu + 1} - \mu - 1}{2\mu\cos(a\kappa)}$$
$$\eta_{aco} = \frac{A_1^{(0)}}{A_2^{(0)}} = \frac{2\mu\cos(a\kappa)}{2\mu + \sqrt{\mu^2 + (4\cos(a\kappa)^2 - 2)\mu + 1} - \mu - 1} \tag{4.7}$$

4.1.2 Dispersion Relation Considering Two Degree-of-Freedom

Dynamical equations for the structure shown in figure 2.2(b) (without considering the transverse spring) are shown below:

$$2m_1\ddot{u}_{j,1} + 2ku_{j,1} - ku_{j,2} - ku_{j-1,2} = 0$$
$$2\mu m_1\ddot{u}_{j,2} + 2ku_{j,2} - ku_{j,1} - ku_{j+1,1} = 0 \tag{4.8}$$

By multiplying equation 4.8 by $\frac{1}{m_1\omega_n^2}$ and considering nondimensional time $\tau = \omega t$, linear natural frequency $\omega_n = \sqrt{k/m_1}$ and nondimensional frequency $\bar{\omega} = \omega/\omega_n$, the following equation in matrix form is obtained:

$$2\bar{\omega}^2 \begin{bmatrix} 1 & 0 \\ 0 & \mu \end{bmatrix} \begin{bmatrix} d^2u_{j,1}/d\tau^2 \\ d^2u_{j,2}/d\tau^2 \end{bmatrix} + \begin{bmatrix} 2 & -1 \\ -1 & 2 \end{bmatrix} \begin{bmatrix} u_{j,1} \\ u_{j,2} \end{bmatrix} + \begin{bmatrix} -u_{j-1,2} \\ -u_{j+1,1} \end{bmatrix} = \begin{bmatrix} 0 \\ 0 \end{bmatrix} \tag{4.9}$$

To solve the system, the asymptotic expansion shown below is used:

$$u_j = u_j^{(0)}, \quad \omega = \omega_0 \tag{4.10}$$

By substituting equation 4.10 into equation 4.9, it is obtained:

$$2\bar{\omega}_0^2 \begin{bmatrix} 1 & 0 \\ 0 & \mu \end{bmatrix} \begin{bmatrix} d^2u_{j,1}^{(0)}/d\tau^2 \\ d^2u_{j,2}^{(0)}/d\tau^2 \end{bmatrix} + \begin{bmatrix} 2 & -1 \\ -1 & 2 \end{bmatrix} \begin{bmatrix} u_{j,1}^{(0)} \\ u_{j,2}^{(0)} \end{bmatrix} + \begin{bmatrix} -u_{j-1,2}^{(0)} \\ -u_{j+1,1}^{(0)} \end{bmatrix} = \begin{bmatrix} 0 \\ 0 \end{bmatrix} \tag{4.11}$$

To solve the system, the following solutions are used:

$$\begin{aligned} \begin{bmatrix} u_{j,1}^{(0)} \\ u_{j,2}^{(0)} \end{bmatrix} &= \begin{bmatrix} (A_1^{(0)}/2)e^{i\kappa a(2j-1)} \\ (A_2^{(0)}/2)e^{i\kappa a(2j)} \end{bmatrix} e^{i\tau} + cc \\ \begin{bmatrix} u_{j\pm1,1}^{(0)} \\ u_{j\pm1,2}^{(0)} \end{bmatrix} &= \begin{bmatrix} (A_1^{(0)}/2)e^{i\kappa a(2(j\pm1)-1)} \\ (A_2^{(0)}/2)e^{i\kappa a(2(j\pm1))} \end{bmatrix} e^{i\tau} + cc \end{aligned} \tag{4.12}$$

By substituting equation 4.12 into equation 4.11, two branches for the linear dispersion are obtained:

$$\begin{aligned} \bar{\omega}_0^{opt} &= \sqrt{\frac{\sqrt{\mu^2 + (4\cos(a\kappa)^2 - 2)\mu + 1} + \mu + 1}{2\mu}} \\ \bar{\omega}_0^{aco} &= \sqrt{\frac{-\sqrt{\mu^2 + (4\cos(a\kappa)^2 - 2)\mu + 1} + \mu + 1}{2\mu}} \end{aligned} \tag{4.13}$$

By Substituting each solution of equation 4.13 into equation 4.11, it is possible to obtain the amplitude ratio for each mode, as shown below:

$$\begin{aligned} \eta_{opt} &= \frac{A_2^{(0)}}{A_1^{(0)}} = \frac{2\mu - \sqrt{\mu^2 + (4\cos(a\kappa)^2 - 2)\mu + 1} - \mu - 1}{2\mu\cos(a\kappa)} \\ \eta_{aco} &= \frac{A_1^{(0)}}{A_2^{(0)}} = \frac{2\mu\cos(a\kappa)}{2\mu + \sqrt{\mu^2 + (4\cos(a\kappa)^2 - 2)\mu + 1} - \mu - 1} \end{aligned} \tag{4.14}$$

By comparing the dispersion relations obtained using a periodic cell with two de-

grees of freedom (equation 4.13) and with three degrees of freedom (equation 4.6), it is possible to verify that both formulations lead to the same result in the linear case, as anticipated in Chapter 2. This equivalence allows for flexibility in choosing the unit cell representation. Therefore, for the nonlinear dispersion relation (Section 4.3), we adopt the cell with two degrees of freedom, as it provides a simpler formulation while preserving the essential dynamics of the infinite structure.

4.2 Bandgap Analysis

Figure 4.1 shows the dispersion relations (infinite structure) and transmissibilities (free finite periodic structure with five cells). Similar characteristics are observed in both responses, including values for both the bandgap and bandstop. Figures 4.1(a), (b), and (c) represent structures with $\mu = 0.5$, $\mu = 1$, and $\mu = 2$, respectively. With $\mu = 1$, there is no bandgap. For $\mu = 0.5$, the bandgap starts at $\omega = 1$, and for $\mu = 2$, the bandgap ends at $\omega = 1$. In other words, with $\mu < 1$, the bandgap is positioned at frequencies above $\omega = 1$, and with $\mu > 1$, the bandgap is positioned at frequencies below $\omega = 1$.

4.3 Dispersion Relation of Nonlinear Periodic Structure

Dynamical equations for the structure shown in figure 2.2(b) are shown below:

$$\begin{aligned} 2m_1\ddot{u}_{j,1} + 2ku_{j,1} - ku_{j,2} - ku_{j-1,2} &= 0 \\ 2\mu m_1\ddot{u}_{j,2} + 2ku_{j,2} - ku_{j,1} - ku_{j+1,1} + \frac{2k_a(L_i - L_0)u_{j,2}}{L_i} + \epsilon\frac{L_0k_au_{j,2}^3}{L_i^3} &= 0 \end{aligned} \tag{4.15}$$

By multiplying equation 4.15 by $\frac{1}{m_1\omega_n^2}$ and considering nondimensional time $\tau = \omega t$, linear natural frequency $\omega_n = \sqrt{k/m_1}$ and nondimensional frequency $\bar{\omega} = \omega/\omega_n$, we can

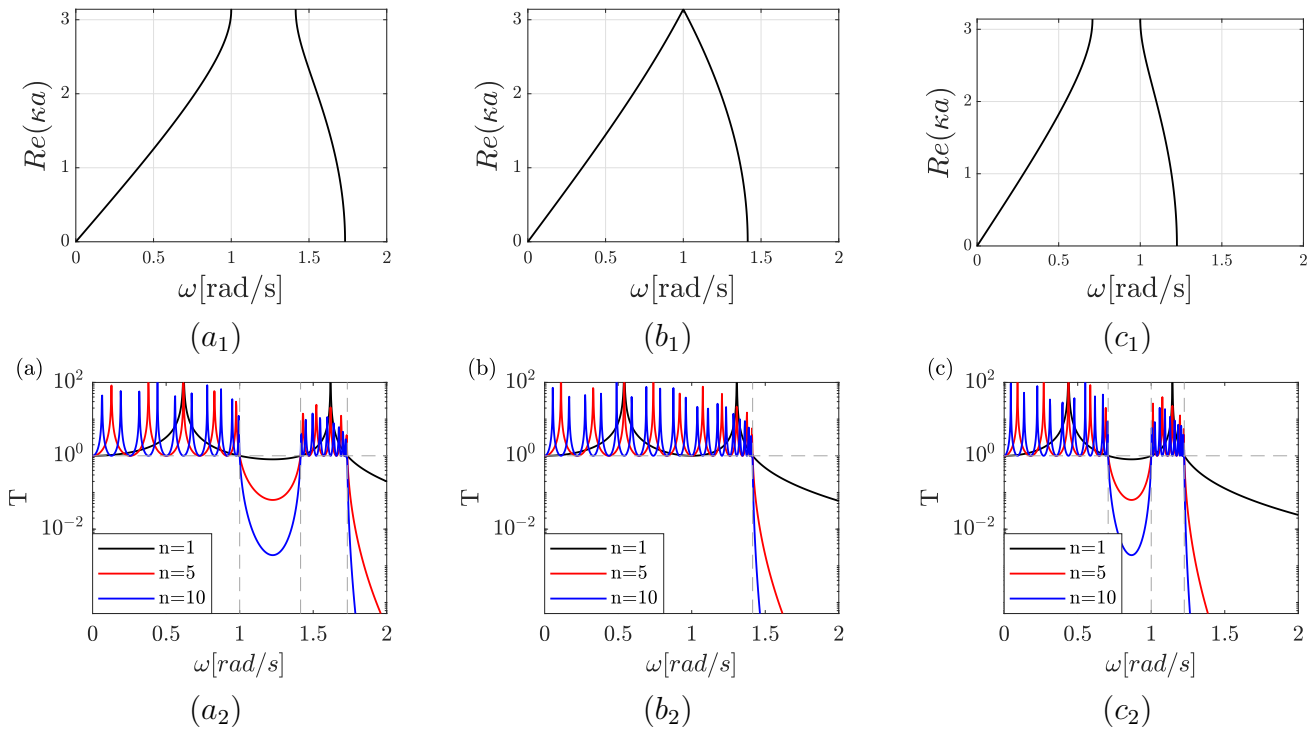

Figure 4.1: Comparison between transmissibility and dispersion relation, where (a) $\mu = 0.5$, (b) $\mu = 1$, and (c) $\mu = 2$. Index 1 indicates dispersion relations, and index 2 indicates transmissibilities.

obtain the following equation in matrix form:

$$2\bar{\omega}^2 \begin{bmatrix} 1 & 0 \\ 0 & \mu \end{bmatrix} \begin{bmatrix} d^2u_{j,1}/d\tau^2 \\ d^2u_{j,2}/d\tau^2 \end{bmatrix} + \begin{bmatrix} 2 & -1 \\ -1 & 2 + \frac{2k_a(L_i - L_0)}{L_i} \end{bmatrix} \begin{bmatrix} u_{j,1} \\ u_{j,2} \end{bmatrix} + \begin{bmatrix} -u_{j-1,2} \\ -u_{j+1,1} \end{bmatrix} + \epsilon \begin{bmatrix} 0 \\ \frac{L_0 k_a u_{j,2}^3}{L_i^3} \end{bmatrix} = \begin{bmatrix} 0 \\ 0 \end{bmatrix} \quad (4.16)$$

To solve the system, the asymptotic expansion shown below is used:

$$u_j = u_j^{(0)} + \epsilon u_j^{(1)} + 0(\epsilon^2), \quad \omega = \omega_0 + \epsilon\omega_1 + 0(\epsilon^2) \quad (4.17)$$

By substituting equation 4.17 into equation 4.16 and equating the coefficients ϵ^0 and

ϵ^1 to zero, it is obtained:

Order ϵ^0:

$$2\bar{\omega}_0^2 \begin{bmatrix} 1 & 0 \\ 0 & \mu \end{bmatrix} \begin{bmatrix} d^2u_{j,1}^{(0)}/d\tau^2 \\ d^2u_{j,2}^{(0)}/d\tau^2 \end{bmatrix} + \begin{bmatrix} 2 & -1 \\ -1 & 2+\frac{2k_a(L_i-L_0)}{L_i} \end{bmatrix} \begin{bmatrix} u_{j,1}^{(0)} \\ u_{j,2}^{(0)} \end{bmatrix} + \begin{bmatrix} -u_{j-1,2}^{(0)} \\ -u_{j+1,1}^{(0)} \end{bmatrix} = \begin{bmatrix} 0 \\ 0 \end{bmatrix} \tag{4.18}$$

Order ϵ^1:

$$2\bar{\omega}_0^2 \begin{bmatrix} 1 & 0 \\ 0 & \mu \end{bmatrix} \begin{bmatrix} d^2u_{j,1}^{(1)}/d\tau^2 \\ d^2u_{j,2}^{(1)}/d\tau^2 \end{bmatrix} + \begin{bmatrix} 2 & -1 \\ -1 & 2+\frac{2k_a(L_i-L_0)}{L_i} \end{bmatrix} \begin{bmatrix} u_{j,1}^{(1)} \\ u_{j,2}^{(1)} \end{bmatrix} + \begin{bmatrix} -u_{j-1,2}^{(1)} \\ -u_{j+1,1}^{(1)} \end{bmatrix} = -4\mu\bar{\omega}_0\bar{\omega}_1 \begin{bmatrix} d^2u_{j,1}^{(0)}/d\tau^2 \\ d^2u_{j,2}^{(0)}/d\tau^2 \end{bmatrix} - \begin{bmatrix} 0 \\ \frac{L_0\bar{k}_a u_{j,2}^3}{L_i^3} \end{bmatrix} \tag{4.19}$$

To solve the system, the following solutions are used:

$$\begin{bmatrix} u_{j,1}^{(0)} \\ u_{j,2}^{(0)} \end{bmatrix} = \begin{bmatrix} (A_1^{(0)}/2)e^{i\kappa a(2j-1)} \\ (A_2^{(0)}/2)e^{i\kappa a(2j)} \end{bmatrix} e^{i\tau} + cc$$
$$\begin{bmatrix} u_{j\pm1,1}^{(0)} \\ u_{j\pm1,2}^{(0)} \end{bmatrix} = \begin{bmatrix} (A_1^{(0)}/2)e^{i\kappa a(2(j\pm1)-1)} \\ (A_2^{(0)}/2)e^{i\kappa a(2(j\pm1))} \end{bmatrix} e^{i\tau} + cc \tag{4.20}$$

By Substituting equation 4.20 into equation 4.18, two two branches for the linear dispersion are obtained:

$$\bar{\omega}_0^2 = \frac{\sqrt{\mu^2 + (4\cos(a\kappa)^2 - 2)\mu + 1 + A} + \mu + 1 + B}{2\mu} \tag{4.21}$$

where

$$A = (2\frac{L_0}{L_i} - 2)k_a\mu + (\frac{L_0}{L_i}^2 - 2\frac{L_0}{L_i} + 1)k_a^2 + (2 - 2\alpha)k_a$$
$$B = (1 - \frac{L_0}{L_i})k_a \tag{4.22}$$

By substituting equation 4.20 into the second component of equation 4.19, it is obtained:

$$2\mu\bar{\omega}_0^2\frac{d^2u_{j,2}^{(1)}}{d\tau^2} + (2 + \frac{2k_a(L_i - L_0)}{L_i})u_{j,2}^{(1)} - u_{j,1}^{(1)} - u_{j+1,1}^{(1)} = d_1e^{2i\kappa ja}e^{i\tau} + d_3e^{6i\kappa ja}e^{3i\tau} + cc \tag{4.23}$$

The term to the left of the equality in equation 4.23 is similar to equation 4.18. Therefore, the terms multiplying $e^{i\tau}$ are secular and must be eliminated. Equation 4.24 shows the term d_1.

$$d_1 = 2A_2^{(0)}\mu\bar{\omega}_0\bar{\omega}_1 - \frac{3(A_2^{(0)})^2\bar{A}_2^{(0)}L_0\bar{k}_a}{16L_i^3} \tag{4.24}$$

By equating the d_1 term to zero, the first-order frequency correction is obtained:

$$\bar{\omega}_1 = \frac{3A_2^{(0)}\bar{A}_2^{(0)}L_0\bar{k}_a}{16L_i^3\mu\bar{\omega}_0} \tag{4.25}$$

By substituting equation 4.25 into second equation 4.17, the resultant dispersion relations for each mode approximated up to the first order are given by:

$$\bar{\omega}_{opt} = \bar{\omega}_0^{opt} + \frac{3\epsilon L_0 \bar{k}_a \mid A_2^{(0)} \mid^2}{16 L_i^3 \mu \bar{\omega}_0^{opt}}$$
$$\bar{\omega}_{aco} = \bar{\omega}_0^{aco} + \frac{3\epsilon L_0 \bar{k}_a \mid A_2^{(0)} \mid^2}{16 L_i^3 \mu \bar{\omega}_0^{aco}} \tag{4.26}$$

Nonlinear dispersion relations are now examined for mass ratios $\mu = 0.5$ and $\mu = 2$, under compression, no prestress, and tension conditions. These results are compared with the transmissibility responses presented in Chapter 3.

Compression Prestress

Figure 4.2 compares the dispersion relations and transmissibility curves for the nonlinear periodic structure under compression prestress. Figures (a) and (b) show the dispersion relations, and (c) and (d) present the corresponding transmissibility results. Figures (a) and (c) refer to the mass ratio $\mu = 0.5$, while (b) and (d) refer to $\mu = 2$. Black curves represent the linear system, while the blue and red curves correspond to the nonlinear system, obtained via continuation: blue for stable and red for unstable branches.

For $\mu = 0.5$, the dispersion relation exhibits an imaginary wavenumber region at low frequencies, indicating wave attenuation due to Bragg scattering. This is consistent with the transmissibility results, which also show attenuation in the same frequency range. For $\mu = 2$, however, the transmissibility curve could not be fully traced using continuation, likely due to increased inertia making the system more prone to numerical difficulties. Despite that, the dispersion relation still indicates attenuation at low frequencies.

In the bandgap region for $\mu = 0.5$, the dispersion relation reveals a reduction in bandgap width, particularly at the upper band edge (optical branch), which suggests a modification in the wave propagation characteristics. Interestingly, the transmissibility shows this reduction primarily at the lower band edge (acoustic branch). This mismatch

may result from numerical limitations or from differences in how effective stiffness is perceived in the wave-based and time-domain analyses.

For $\mu = 2$, the dispersion relation indicates a widening of the bandgap, with a shift in the acoustic branch, while the optical branch remains mostly unchanged. In contrast, the transmissibility curve suggests a narrower bandgap, although its interpretation is complicated by the presence of unstable branches, which obscure the exact band edges.

These comparisons underscore the importance of combining dispersion analysis and transmissibility computations to capture the full dynamics of nonlinear periodic structures. While dispersion relations provide insight into wave propagation and Bragg scattering mechanisms, transmissibility reflects how these features manifest in the system's response under finite, possibly large, excitations—particularly when geometric nonlinearities and changes in effective stiffness are present due to prestress conditions.

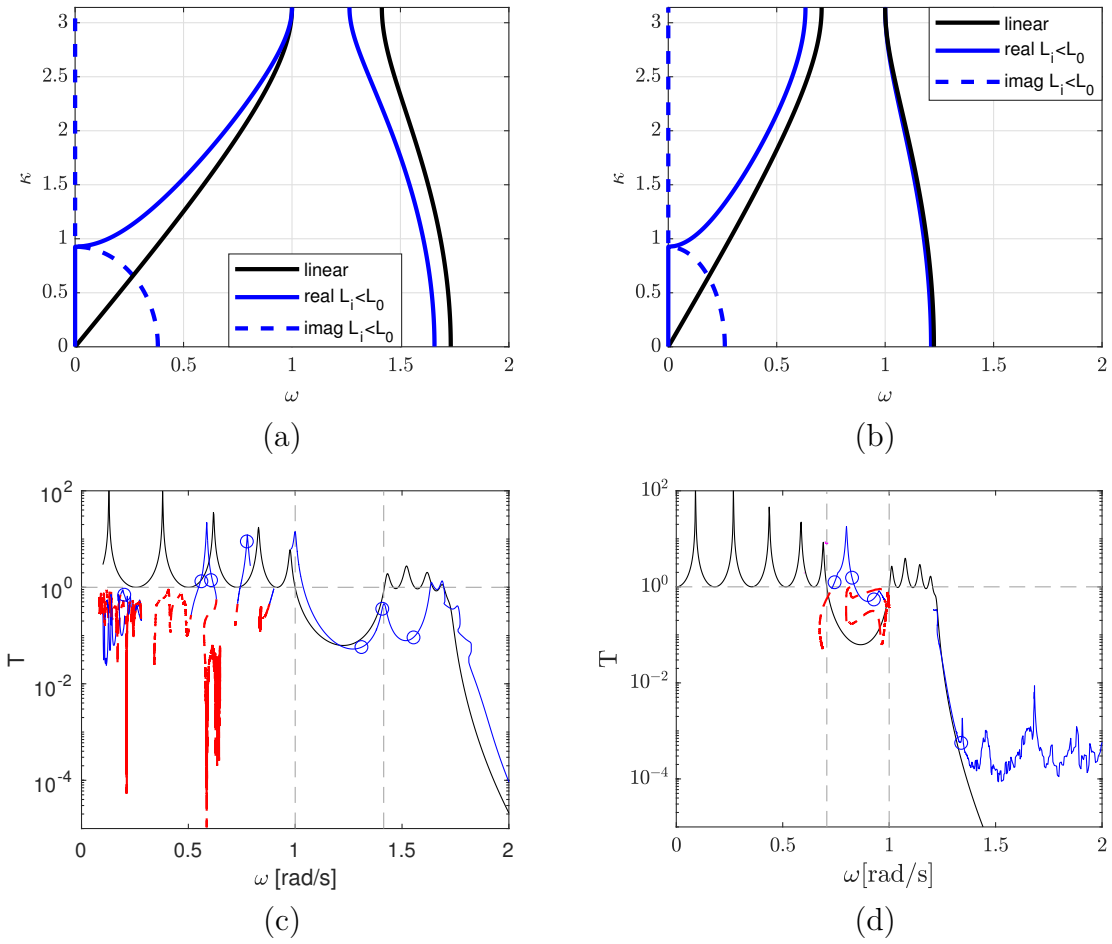

Figure 4.2: Dispersion relations and transmissibility curves for the nonlinear periodic structure under compressive prestress. (a) Dispersion relation for $\mu = 0.5$; (b) dispersion relation for $\mu = 2$; (c) transmissibility for $\mu = 0.5$; (d) transmissibility for $\mu = 2$. Black curves represent the linear response, blue curves represent the nonlinear response and red curves in (c) and (d) denote unstable solutions obtained via continuation and blue circles denote the transmissibility obtained through fourth-order Runge–Kutta method.

No Prestress

Figure 4.3 compares the dispersion relations and transmissibility curves for the nonlinear periodic structure without prestress. Figures (a) and (b) show the dispersion relations, while (c) and (d) present the corresponding transmissibility results. Figures (a) and (c) refer to the mass ratio $\mu = 0.5$, and (b) and (d) refer to $\mu = 2$. Black curves represent the linear system, while the magenta and red curves correspond to the nonlinear system obtained via numerical continuation: magenta indicates stable branches, and red unstable ones. In the dispersion relations, the magenta and gray curves represent nonlinear dispersion for amplitudes $A_2 = 1$ and $A_2 = 100$, respectively, highlighting the system's amplitude-dependent behaviour.

In both cases ($\mu = 0.5$ and $\mu = 2$), the transmissibility curves show a reduction in the bandgap width and increased attenuation at low frequencies. This indicates that the system becomes more transparent to wave propagation within the original bandgap range when nonlinearities are present.

To observe noticeable differences between the linear and nonlinear dispersion relations, it was necessary to increase the oscillation amplitude A_2. With higher amplitude ($A_2 = 100$), the nonlinear dispersion relation deviates significantly from the linear one, especially in the low-frequency region, where a gap with no real wavenumber appears (an indication of wave attenuation). This is consistent with the emergence of locally resonant bandgaps due to geometric nonlinearity.

Moreover, increasing the amplitude causes the entire bandgap to shift toward higher frequencies, affecting both the acoustic and optical branches. This upward shift reflects a hardening-type behaviour, where the effective stiffness of the system increases with amplitude. This is a hallmark of nonlinear dispersion, in contrast to linear systems where bandgaps are fixed by geometry and mass distribution.

These findings illustrate the fundamental difference between frequency-domain predictions (dispersion relation) and steady-state forced responses (transmissibility). While

dispersion relations provide valuable insight into wave propagation and attenuation zones, transmissibility reveals how the system responds to external excitation, especially when nonlinear effects alter the dynamics in amplitude-dependent ways.

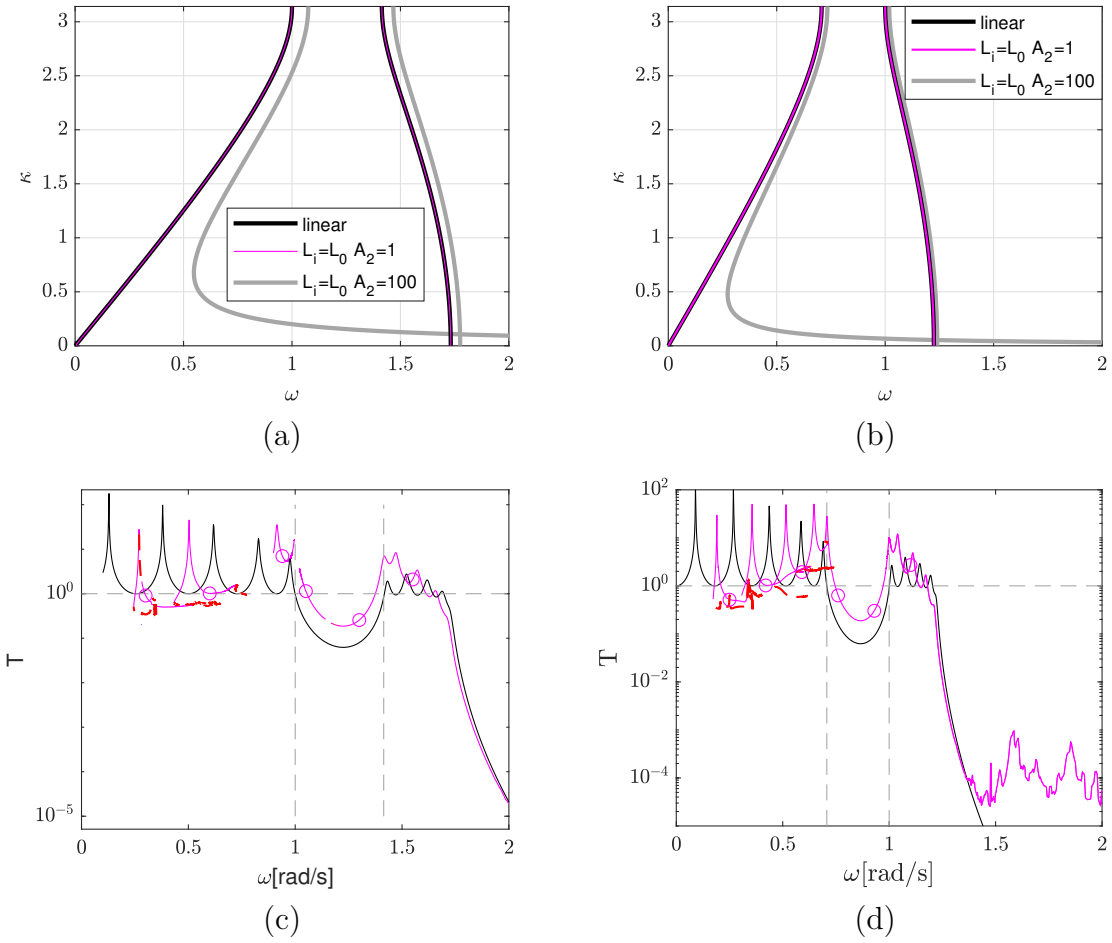

Figure 4.3: Dispersion relations and transmissibility curves for the nonlinear periodic structure without prestress. (a) Dispersion relation for $\mu = 0.5$; (b) dispersion relation for $\mu = 2$; (c) transmissibility for $\mu = 0.5$; (d) transmissibility for $\mu = 2$. Black curves represent the linear response. In (a) and (b), magenta and gray curves correspond to nonlinear dispersion relations with amplitude values $A_2 = 1$ and $A_2 = 100$, respectively, highlighting the amplitude-dependent behaviour. In (c) and (d), magenta curves show the nonlinear transmissibility and red curves denote unstable branches obtained via continuation; and magenta circles indicate the nonlinear transmissibility obtained through the fourth-order Runge–Kutta method.

Tension Prestress

Figure 4.4 compares the dispersion relations and transmissibility curves for the nonlinear periodic structure under tension prestress. Figures (a) and (b) show the dispersion relations, and (c) and (d) present the corresponding transmissibility results. Figures (a) and (c) refer to the mass ratio $\mu = 0.5$, while (b) and (d) refer to $\mu = 2$. Black curves represent the linear system, while the green and red curves correspond to the nonlinear system, obtained via continuation: blue for stable and red for unstable branches.

In both mass ratio cases, the dispersion relations reveal attenuation at low frequencies, as indicated by the absence of real wavenumber solutions in this region. This behaviour is consistent with the transmissibility curves, although for $\mu = 0.5$, the continuation method failed to complete the response curve due to numerical limitations.

Regarding the bandgap characteristics, for $\mu = 0.5$, the transmissibility shows a shift of the bandgap toward higher frequencies, which is also observed in the nonlinear dispersion relation—indicating a stiffening (hardening-type) effect due to tension prestress. This shift reflects an increase in the effective stiffness, which raises the natural frequencies of the system.

For $\mu = 2$, the transmissibility curve shows a reduction in the bandgap width across both the acoustic and optical branches, suggesting a more compliant system response under tension prestress at higher mass ratios. However, the nonlinear dispersion relation for $\mu = 2$ shows that this reduction is limited to the optical branch, with the acoustic branch remaining nearly unchanged. This discrepancy between the two methods may arise from differences in excitation and boundary conditions, or from the localized and global nature of wave propagation and response in nonlinear systems.

These results underscore the influence of mass ratio and prestress on the dynamic behaviour of the system, especially in how they affect the formation and shifting of bandgaps through changes in inertia and stiffness coupling mechanisms.

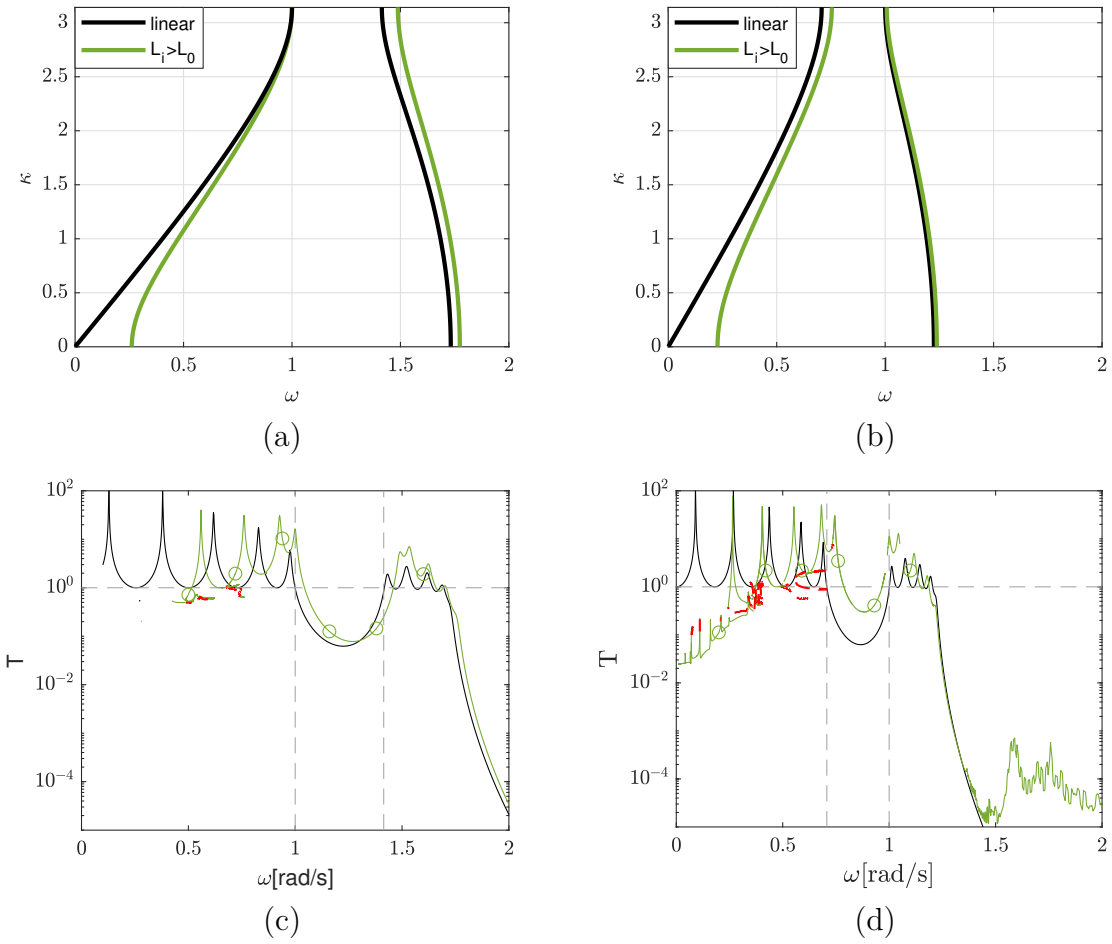

Figure 4.4: Dispersion relations and transmissibility curves for the nonlinear periodic structure under tension prestress. (a) Dispersion relation for $\mu = 0.5$; (b) dispersion relation for $\mu = 2$; (c) transmissibility for $\mu = 0.5$; (d) transmissibility for $\mu = 2$. Black curves represent the linear response, green curves represent the nonlinear response and red curves in (c) and (d) denote unstable solutions obtained via continuation and green circles denote the transmissibility obtained through fourth-order Runge–Kutta method.

Chapter 5

CONCLUSIONS

In this chapter, final remarks regarding the periodic structure investigated throughout the thesis are presented.

The linear analysis revealed how classical bandgap behaviour in periodic structures is governed by both the mass ratio and the number of unit cells. While the bandgap region is already present for a single cell, its attenuation becomes more pronounced as the number of cells increases, illustrating the cumulative effect of periodicity. The bandgap limits remain approximately fixed regardless of system size, as they are closely linked to the natural frequencies of the unit cell.

Additionally, the mass ratio plays a central role in the bandgap location. A symmetric configuration with equal masses does not produce attenuation, whereas variations in the mass ratio shift the bandgap to higher or lower frequencies.

In the nonlinear periodic structure, the responses show strong sensitivity to initial conditions, manifesting a wide range of behaviours, including periodic, quasi-periodic, and chaotic regimes. Tools such as basins of attraction, Poincaré sections, Lyapunov exponents, and time-domain simulations enabled the identification and classification of these dynamic responses.

When investigating the influence of prestress, it was found that compression prestress introduces significant changes in the system's dynamics. Notably, the equilibrium

shifts away from zero, a behaviour not present in the no-prestress and tension cases. Under compression, the structure tends to exhibit a higher prevalence of chaotic and quasi-periodic responses, particularly at low excitation frequencies. This is attributed to the amplified effects of geometric nonlinearity and increased by sensitivity to initial conditions. For instance, with $\mu = 0.5$ and excitation frequency $\omega = 0.3$ [rad/s], the basin of attraction shows a mixed distribution of chaotic and periodic responses, suggesting comparable probabilities of each regime. The interlaced nature of these solutions makes the system's long-term behaviour difficult to predict. In contrast, other compression scenarios show a predominance of a single regime - periodic, quasi-periodic, or chaotic—resulting in increased predictability.

For $\mu = 0.5$, the transmissibility curve exhibited unstable branches. For $\mu = 2$, transmissibility could not be computed at low frequencies due to numerical issues in the continuation method. Physically, increasing $\mu = m_2/m_1$ enhances the inertia contribution of internal resonators, increasing the effective degrees of freedom and amplifying the impact of internal nonlinear behaviour. This promotes stronger energy exchange and enables more complex internal dynamics, potentially favoring chaotic behaviour.

Under compression prestress, both mass ratios showed a reduction in the bandgap region. This is a direct consequence of the softening behaviour introduced by geometric nonlinearities, which reduces the effective stiffness. Consequently, wave propagation characteristics are altered, and the Bragg scattering conditions shift, affecting both acoustic and optical branches.

In the absence of prestress, the system still exhibits attenuation at low frequencies, indicating the presence of localized modes or internal resonance. This phenomenon is observed for both mass ratios and is linked to an increase in effective stiffness and the inherent energy redistribution within the structure. To detect shifts in the nonlinear dispersion curves, it was necessary to increase the amplitude A_2, highlighting the amplitude-dependent nature of wave propagation. Dynamically, this prestress condition leads to fewer chaotic responses and a predominance of periodic or quasi-periodic

behaviours, all with equilibria centred around zero. As the excitation frequency ω increases, quasi-periodic responses become more likely. Periodic solutions, present mainly at lower frequencies, tend to decrease in amplitude and prevalence with increasing frequency. This trend is reflected in the basins of attraction, where quasi-periodic regions gradually expand and occupy more of the phase space.

With tension prestress, attenuation at low frequencies remains evident for both mass ratios. However, different shifts in the bandgap behaviour are observed: for $\mu = 0.5$, the bandgap moves to higher frequencies, consistent with the hardening-type behaviour that increases effective stiffness. For $\mu = 2$, the bandgap region reduces in width. The effective increase in stiffness under tension raises the natural frequencies, which may explain the upward shift of bandgaps and the reduction of nonlinear dynamic irregularities. The responses in this case tend to be more periodic, suggesting increased stability under tension prestress. In this case, the basins are entirely filled with periodic solutions, featuring high amplitudes at low frequencies and lower amplitudes as frequency increases. Periodic behaviour dominates the phase space, suggesting high predictability and robustness.

In conclusion, the application of different prestress states proves to be an effective strategy for attenuating axial vibrations at low frequencies and for modifying the location and extent of bandgap regions in periodic structures.

5.1 Scientific Contributions

- VASCONCELLOS, D. P.; CRUZ, R.; FERNANDES, J.; SILVEIRA, M. Vibration attenuation and energy harvesting in metastructures with nonlinear absorbers conserving mass and strain energy. The European Physical Journal Special Topics, Springer, v. 231, n. 8, p. 1393–1401, 2022.

- VASCONCELLOS, D. P.; SILVEIRA, M. Optimization of axial vibration attenuation of periodic structure with nonlinear stiffness without addition of mass.

Journal of Vibration and Acoustics, American Society of Mechanical Engineers, v. 142, n. 6, p. 061009, 2020.

- VASCONCELLOS, D. P.; CRUZ, R. S. ; FERNANDES, J. C. M. ; Silveira, M. . Axial vibration attenuation and energy harvesting with nonlinear absorbers without addition of mass. In: International Conference on Advances in Energy Harvesting Technology ICAEHT, 2021, Lublin. International Conference on Advances in Energy Harvesting Technology ICAEHT 2021, 2021.

- VASCONCELLOS, D. P.; Silveira, M. . Band gap and modal interaction analysis of metastructures with high-staticlow-dynamic stiffness with multiple scales. In: 42nd Ibero-Latin-American Congress on Computational Methods in Engineering (XLII CILAMCE), 2021, Rio de Janeiro. Proceedings of the Ibero-Latin-American Congress on Computational Methods in Engineering, 2021.

- VASCONCELLOS, D. P.; Silveira, M. . Wave propagation in one-dimensional diatomic metastructure with high-static-low-dynamic stiffness. In: XLIII CILAMCE, 2022, Foz do Iguaçu. Proceedings of the Ibero-Latin-American Congress on Computational Methods in Engineering, 2022.

5.2 Future Work Suggestions

Based on the findings of this study, the following directions are suggested for future research:

- Extension to Higher-Dimensional Systems: Investigating two- and three-dimensional periodic structures could reveal richer dynamics, including mode coupling, directional bandgaps, and anisotropic wave propagation phenomena;

- Experimental Validation: Physical prototyping and testing of structures with controllable prestress could validate the numerical predictions, particularly regarding

nonlinear dispersion behaviour, chaotic regimes, and bandgap shifts;

- Inclusion of Damping Effects: Investigate the influence of damping by incorporating different models, such as viscous, structural, or nonlinear damping, to better understand its effect on system stability, energy dissipation, and the characteristics of attenuation zones;

- Optimisation for Vibration Isolation or Energy Harvesting: The insights gained in this thesis can be applied to the design and optimisation of periodic structures aimed at vibration mitigation or energy harvesting, where tuning bandgaps through prestress and nonlinearity is beneficial.

REFERENCES

BAE, M. H.; OH, J. H. Nonlinear elastic metamaterial for tunable bandgap at quasi-static frequency. *Mechanical Systems and Signal Processing*, Elsevier, v. 170, p. 108832, 2022.

BOECHLER, N.; DARAIO, C.; NARISETTI, R. K.; RUZZENE, M.; LEAMY, M. Analytical and experimental analysis of bandgaps in nonlinear one dimensional periodic structures. In: SPRINGER. *IUTAM Symposium on Recent Advances of Acoustic Waves in Solids*. [S.l.], 2010. p. 209—-219.

BRILLOUIN, L. Wave propagation in periodic structures. MGH, 1946.

CARNEIRO, J.; BRENNAN, M.; GONÇALVES, P.; CLEANTE, V.; BUENO, D.; SANTOS, R. On the attenuation of vibration using a finite periodic array of rods comprised of either symmetric or asymmetric cells. *Journal of Sound and Vibration*, Elsevier, v. 511, p. 116217, 2021.

CARRELLA, A.; BRENNAN, M.; WATERS, T. Static analysis of a passive vibration isolator with quasi-zero-stiffness characteristic. *Journal of sound and vibration*, Elsevier, v. 301, n. 3-5, p. 678—-689, 2007.

CARRELLA, A.; BRENNAN, M. J.; KOVACIC, I.; WATERS, T. P. On the force transmissibility of a vibration isolator with quasi-zero-stiffness. *Journal of Sound and Vibration*, Elsevier, v. 322, n. 4-5, p. 707—-717, 2009.

CHAKRABORTY, G.; MALLIK, A. Dynamics of a weakly non-linear periodic chain. *International Journal of Non-Linear Mechanics*, Elsevier, v. 36, n. 2, p. 375—-389, 2001.

CHENG, C.; LI, S.; WANG, Y.; JIANG, X. Force and displacement transmissibility of a quasi-zero stiffness vibration isolator with geometric nonlinear damping. *Nonlinear Dynamics*, Springer, v. 87, p. 2267—-2279, 2017.

CROËNNE, C.; LEE, E.; HU, H.; PAGE, J. Band gaps in phononic crystals: Generation mechanisms and interaction effects. *AIP Advances*, AIP Publishing, v. 1, n. 4, 2011.

DATSERIS, G.; WAGEMAKERS, A. Effortless estimation of basins of attraction. *Chaos: An Interdisciplinary Journal of Nonlinear Science*, AIP Publishing, v. 32, n. 2, 2022.

DAZA, A.; WAGEMAKERS, A.; SANJUÁN, M. A. Classifying basins of attraction using the basin entropy. *Chaos, Solitons & Fractals*, Elsevier, v. 159, p. 112112, 2022.

DHOOGE, A.; GOVAERTS, W.; KUZNETSOV, Y. A.; MEIJER, H. G. E.; SAUTOIS, B. New features of the software MatCont for bifurcation analysis of dynamical systems. *Mathematical and Computer Modelling of Dynamical Systems*, Taylor & Francis, v. 14, n. 2, p. 147—-175, 2008.

DING, Y.; MAGNUSSON, R. Band gaps and leaky-wave effects in resonant photonic-crystal waveguides. *Optics express*, OSA, v. 15, n. 2, p. 680—-694, 2007.

GONÇALVES, P.; BRENNAN, M.; CLEANTE, V. Predicting the stop-band behaviour of finite mono-coupled periodic structures from the transmissibility of a single element. *Mechanical Systems and Signal Processing*, Elsevier, v. 154, p. 107512, 2021.

HAO, Z.; CAO, Q. The isolation characteristics of an archetypal dynamical model with stable-quasi-zero-stiffness. *Journal of sound and vibration*, Elsevier, v. 340, p. 61—-79, 2015.

HAO, Z.; CAO, Q.; WIERCIGROCH, M. Nonlinear dynamics of the quasi-zero-stiffness sd oscillator based upon the local and global bifurcation analyses. *Nonlinear Dynamics*, Springer, v. 87, p. 987—-1014, 2017.

HOBECK, J. D.; INMAN, D. J. Magnetoelastic metastructures for passive broadband vibration suppression. In: INTERNATIONAL SOCIETY FOR OPTICS AND PHOTONICS. *Active and Passive Smart Structures and Integrated Systems 2015*. [S.l.], 2015. v. 9431, p. 943119.

HOBECK, J. D.; LAURANT, C.; INMAN, D. J. 3d printing of metastructures for passive broadband vibration suppression. In: *20th International Conference on Composite Materials, Denmark, Copenhagen*. [S.l.: s.n.], 2015. p. 19—-24.

HUANG, N. E.; SHEN, Z.; LONG, S. R.; WU, M. C.; SHIH, H. H.; ZHENG, Q.; YEN, N.-C.; TUNG, C. C.; LIU, H. H. The empirical mode decomposition and the hilbert spectrum for nonlinear and non-stationary time series analysis. *Proceedings of the Royal Society of London. Series A: mathematical, physical and engineering sciences*, The Royal Society, v. 454, n. 1971, p. 903—-995, 1998.

HUSSEIN, M. I.; LEAMY, M. J.; RUZZENE, M. Dynamics of phononic materials and structures: Historical origins, recent progress, and future outlook. *Applied Mechanics Reviews*, American Society of Mechanical Engineers, v. 66, n. 4, p. 040802, 2014.

INMAN, D. J.; SINGH, R. C. *Engineering vibration*. [S.l.]: Prentice Hall Englewood Cliffs, NJ, 1994. v. 3.

INOUYE, T.; SHINOSAKI, K.; SAKAMOTO, H.; TOI, S.; UKAI, S.; IYAMA, A.; KATSUDA, Y.; HIRANO, M. Quantification of EEG irregularity by use of the entropy of the power spectrum. *Electroencephalography and clinical neurophysiology*, Elsevier, v. 79, n. 3, p. 204—-210, 1991.

IQBAL, M.; KUMAR, A.; JAYA, M. M.; BURSI, O. S. Flexural band gaps and vibration control of a periodic railway track. *Scientific Reports*, Nature Publishing Group UK London, v. 11, n. 1, p. 18145, 2021.

KITTEL, C.; MCEUEN, P. *Introduction to solid state physics*. [S.l.]: John Wiley & Sons, 2018.

KRÖDEL, S.; THOMÉ, N.; DARAIO, C. Wide band-gap seismic metastructures. *Extreme Mechanics Letters*, Elsevier, v. 4, p. 111—-117, 2015.

LAMARQUE, C. H.; SAVADKOOHI, A. T.; CHARLEMAGNE, S. Experimental results on the vibratory energy exchanges between a linear system and a chain of nonlinear oscillators. *Journal of Sound and Vibration*, Elsevier, v. 437, p. 97—-109, 2018.

LEDEZMA-RAMIREZ, D. F.; FERGUSON, N. S.; BRENNAN, M. J.; TANG, B. An experimental nonlinear low dynamic stiffness device for shock isolation. *Journal of Sound and Vibration*, Elsevier, v. 347, p. 1—-13, 2015.

LENCI, S.; REGA, G.; RUZZICONI, L. The dynamical integrity concept for interpreting/predicting experimental behaviour: from macro-to nano-mechanics. *Philosophical Transactions of the Royal Society A: Mathematical, Physical and Engineering Sciences*, The Royal Society Publishing, v. 371, n. 1993, p. 20120423, 2013.

MA, Z.; ZHOU, R.; YANG, Q. Recent advances in quasi-zero stiffness vibration isolation systems: an overview and future possibilities. *Machines*, MDPI, v. 10, n. 9, p. 813, 2022.

MANKTELOW, K. L. *Dispersion analysis of nonlinear periodic structures*. Tese (Doutorado) — Georgia Institute of Technology, 2013.

MARATHE, A.; CHATTERJEE, A. Wave attenuation in nonlinear periodic structures using harmonic balance and multiple scales. *Journal of Sound and Vibration*, Elsevier, v. 289, n. 4-5, p. 871—-888, 2006.

MEAD, D. Wave propagation in continuous periodic structures: research contributions from southampton, 1964–1995. *Journal of sound and vibration*, Elsevier, v. 190, n. 3, p. 495—-524, 1996.

MEAUD, J. Nonlinear wave propagation and dynamic reconfiguration in two-dimensional lattices with bistable elements. *Journal of Sound and Vibration*, Elsevier, v. 473, p. 115239, 2020.

NARISETTI, R. K.; LEAMY, M. J.; RUZZENE, M. A perturbation approach for predicting wave propagation in one-dimensional nonlinear periodic structures. *Journal of Vibration and Acoustics*, American Society of Mechanical Engineers Digital Collection, v. 132, n. 3, 2010.

NAYFEH, A. H.; BALACHANDRAN, B. *Applied nonlinear dynamics: analytical, computational, and experimental methods*. [S.l.]: John Wiley & Sons, 2008.

NIU, F.; MENG, L.; WU, W.; SUN, J.; ZHANG, W.; MENG, G.; RAO, Z. Design and analysis of a quasi-zero stiffness isolator using a slotted conical disk spring as negative stiffness structure. *Journal of Vibroengineering*, JVE International Ltd., v. 16, n. 4, p. 1769—-1785, 2014.

ORLANDO, D.; GONÇALVES, P. B.; REGA, G.; LENCI, S. Influence of transient escape and added load noise on the dynamic integrity of multistable systems. *International Journal of Non-Linear Mechanics*, Elsevier, v. 109, p. 140—-154, 2019.

OUDICH, M.; GERARD, N. J.; DENG, Y.; JING, Y. Tailoring structure-borne sound through bandgap engineering in phononic crystals and metamaterials: a comprehensive review. *Advanced Functional Materials*, Wiley Online Library, v. 33, n. 2, p. 2206309, 2023.

POPA, B.-I.; CUMMER, S. A. Non-reciprocal and highly nonlinear active acoustic metamaterials. *Nature communications*, Nature Publishing Group, v. 5, p. 3398, 2014.

RAO, S. *Mechanical Vibrations*. [S.l.]: Prentice Hall, 2011. (Always learning). ISBN 9789810687120.

ROMEO, F.; REGA, G. Periodic and localized solutions in chains of oscillators with softening or hardening cubic nonlinearity. *Meccanica*, Springer, v. 50, n. 3, p. 721—-730, 2015.

ROTHOS, V.; VAKAKIS, A. Dynamic interactions of traveling waves propagating in a linear chain with an local essentially nonlinear attachment. *Wave Motion*, Elsevier, v. 46, n. 3, p. 174—-188, 2009.

SOLIMAN, M.; THOMPSON, J. Integrity measures quantifying the erosion of smooth and fractal basins of attraction. *Journal of Sound and Vibration*, Elsevier, v. 135, n. 3, p. 453—-475, 1989.

SUGINO, C.; ERTURK, A. Analysis of multifunctional piezoelectric metastructures for low-frequency bandgap formation and energy harvesting. *Journal of Physics D: Applied Physics*, IOP Publishing, v. 51, n. 21, p. 215103, 2018.

SUGINO, C.; RUZZENE, M.; ERTURK, A. Merging mechanical and electromechanical bandgaps in locally resonant metamaterials and metastructures. *Journal of the Mechanics and Physics of Solids*, Elsevier, v. 116, p. 323—-333, 2018.

SUGINO, C.; XIA, Y.; LEADENHAM, S.; RUZZENE, M.; ERTURK, A. A general theory for bandgap estimation in locally resonant metastructures. *Journal of Sound and Vibration*, Elsevier, v. 406, p. 104—-123, 2017.

SUI, G.; ZHANG, X.; HOU, S.; SHAN, X.; HOU, W.; LI, J. Quasi-zero stiffness isolator suitable for low-frequency vibration. *Machines*, MDPI, v. 11, n. 5, p. 512, 2023.

TANG, B.; BRENNAN, M. J. On the shock performance of a nonlinear vibration isolator with high-static-low-dynamic-stiffness. *International Journal of Mechanical Sciences*, Elsevier, v. 81, p. 207—-214, 2014.

VAKAKIS, A. F.; KING, M. Resonant oscillations of a weakly coupled, nonlinear layered system. *Acta mechanica*, Springer, v. 128, n. 1-2, p. 59—-80, 1998.

VASCONCELLOS, D.; CRUZ, R.; FERNANDES, J.; SILVEIRA, M. Vibration attenuation and energy harvesting in metastructures with nonlinear absorbers conserving mass and strain energy. *The European Physical Journal Special Topics*, Springer, v. 231, n. 8, p. 1393—-1401, 2022.

VASCONCELLOS, D. P.; SILVEIRA, M. Optimization of axial vibration attenuation of periodic structure with nonlinear stiffness without addition of mass. *Journal of Vibration and Acoustics*, American Society of Mechanical Engineers, v. 142, n. 6, p. 061009, 2020.

VESELAGO, V. G. The electrodynamics of substances with simultaneously negative values of ϵ and μ. *Soviet physics uspekhi*, IOP Publishing, v. 10, n. 4, p. 509, 1968.

WANG, K.; ZHOU, J.; XU, D.; OUYANG, H. Lower band gaps of longitudinal wave in a one-dimensional periodic rod by exploiting geometrical nonlinearity. *Mechanical Systems and Signal Processing*, Elsevier, v. 124, p. 664—-678, 2019.

XIAO, L.; SUN, X.; CHENG, L.; YU, X. A 3d-printed quasi-zero-stiffness isolator for low-frequency vibration isolation: Modelling and experiments. *Journal of Sound and Vibration*, Elsevier, v. 577, p. 118308, 2024.

XU, D.; YU, Q.; ZHOU, J.; BISHOP, S. Theoretical and experimental analyses of a nonlinear magnetic vibration isolator with quasi-zero-stiffness characteristic. *Journal of sound and vibration*, Elsevier, v. 332, n. 14, p. 3377—-3389, 2013.

YAO, S.; ZHOU, X.; HU, G. Experimental study on negative effective mass in a 1d mass–spring system. *New Journal of Physics*, IOP Publishing, v. 10, n. 4, p. 043020, 2008.

YOUNESIAN, D.; SADRI, M.; ESMAILZADEH, E. Primary and secondary resonance analyses of clamped–clamped micro-beams. *Nonlinear dynamics*, Springer, v. 76, p. 1867—-1884, 2014.

YUN, Y.; MIAO, G.; ZHANG, P.; HUANG, K.; WEI, R. Nonlinear acoustic wave propagating in one-dimensional layered system. *Physics Letters A*, Elsevier, v. 343, n. 5, p. 351—-358, 2005.

ZHU, R.; LIU, X.; HU, G.; SUN, C.; HUANG, G. A chiral elastic metamaterial beam for broadband vibration suppression. *Journal of Sound and Vibration*, Elsevier, v. 333, n. 10, p. 2759—-2773, 2014.